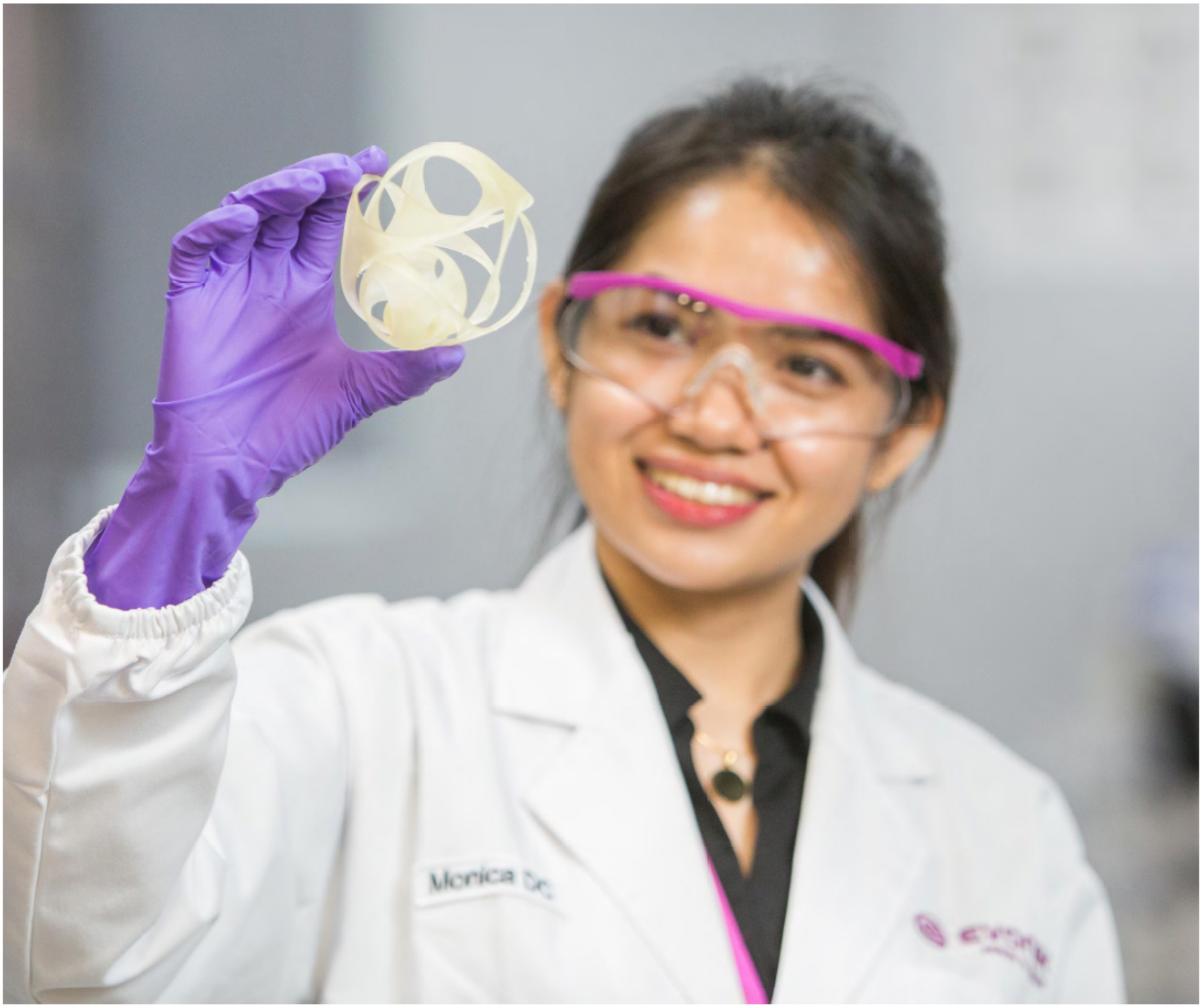

Pushing the boundaries of chemistry?
It takes
#HumanChemistry

Make your curiosity and talent as a chemist matter to the world with a specialty chemicals leader. Together, we combine cutting-edge science with engineering expertise to create solutions that answer real-world problems. Find out how our approach to technology creates more opportunities for growth, and see what chemistry can do for you at:

evonik.com/career

EVONIK
Leading Beyond Chemistry

ADVANCED FUNCTIONAL MATERIALS
www.afm-journal.de

Check for updates

3D Bioprinting of Miniaturized Tissues Embedded in Self-Assembled Nanoparticle-Based Fibrillar Platforms

Syeda M. Bakht, Manuel Gomez-Florit, Tara Lamers, Rui L. Reis, Rui M. A. Domingues, and Manuela E. Gomes**

The creation of microphysiological systems like tissue and organ-on-chip for in vitro modeling of human physiology and diseases is gathering increasing interest. However, the platforms used to build these systems have limitations concerning implementation, automation, and cost-effectiveness. Moreover, their typical plastic-based housing materials are poor recreations of native tissue extracellular matrix (ECM) and barriers. Here, the controlled self-assembly of plant-derived cellulose nanocrystals (CNC) is combined with the concept of 3D bioprinting in suspension baths for the direct biofabrication of microphysiological systems embedded within an ECM mimetic fibrillar support material. The developed support CNC fluid gel allows exceptionally high-resolution bioprinting of 3D constructs with arbitrary geometries and low restrictions of bioink choice. The further induction of CNC self-assembly with biocompatible calcium ions results in a transparent biomimetic nanoscaled fibrillar matrix that allows hosting different compartmentalized cell types and perfusable channels, has tailored permeability for biomacromolecules diffusion and cellular crosstalk, and holds structural stability to support long-term in vitro cell maturation. In summary, this xeno-free nanoscale CNC fibrillar matrix allows the biofabrication of hierarchical living constructs, opening new opportunities not only for developing physiologically relevant 3D in vitro models but also for a wide range of applications in regenerative medicine.

1. Introduction

Progress of tissue engineering is being leveraged to advance several other interface biomedical fields and applications. One example is the development of in vitro 3D tissue and disease models with the improved potential to simulate native tissue/organ behavior, when compared to 2D cell monolayer cultures or even animal models, yielding drug responses with higher similarity to those of human tissues.[1] Organ/tissue-on-chip (OoC) technology, in particular, has seen increasing interest in the development of microphysiological systems with improved predictive power for their in vitro–in vivo extrapolations.[2] Although still in its infancy, this technology is developing rapidly in order to meet the increasing demands for reducing animal testing in basic research as well as in drug development processes.[3,4] However, the complexities of organ functions are difficult to model in these systems. Many different fabrication approaches have been devised in terms of model complexity and device designs.[3] Among the most successful platforms currently translated into commercial products are those known as tissue plates, consisting of arrays of tissue chips for on-plate replicates.[5] Similar to the majority of other OoC platforms, these plates are based on predefined sample housing circuits made of transparent polymeric materials such as poly(methyl methacrylate) or polydimethylsiloxane (PDMS).[6,7] Despite mitigating the issue of sample replicate throughput, such platforms tend to sacrifice the potential to recreate the cell–cell and cell–extracellular matrix (ECM) cross-talk existing in living organisms. In vivo, parenchyma and its corresponding stromal tissues are primarily made of non-cellular interstitial fibrillar ECM that support the function of the cellular constituents.[8] Cells and ECM are hierarchically organized by basement membranes (BM) that divide them into compartments.[9] Structurally, this specialized form of ECM consists of dense 3D fibrillar networks that, despite having a tissue-specific composition, conserve their nanoscale topographical features across anatomical locations.[10,11] Beyond the signaling derived from the biochemical nature of their components, the biophysical cues stemming from the nanoscale supramolecular organization of ECM and BM have a far more important biological function than simply providing structural support for cells.[9,12] These fibrillar architectures of ECMs convey mechanical and topological signals that have many recognized roles in the regulation of important cellular mechanisms such as migration,

---

S. M. Bakht, M. Gomez-Florit, T. Lamers, R. L. Reis, R. M. A. Domingues, M. E. Gomes
3B's Research Group I3Bs—Research Institute on Biomaterials Biodegradables and Biomimetics University of Minho Headquarters of the European Institute of Excellence on Tissue Engineering and Regenerative Medicine AvePark - Parque de Ciência e Tecnologia Zona Industrial da Gandra Barco
Guimarães 4805-017, Portugal
E-mail: rui.domingues@i3bs.uminho.pt; megomes@i3bs.uminho.pt
S. M. Bakht, M. Gomez-Florit, T. Lamers, R. L. Reis, R. M. A. Domingues, M. E. Gomes
ICVS/3B's-PT Government Associate Laboratory
Braga/Guimarães 4805-017, Portugal

The ORCID identification number(s) for the author(s) of this article can be found under https://doi.org/10.1002/adfm.202104245.

DOI: 10.1002/adfm.202104245

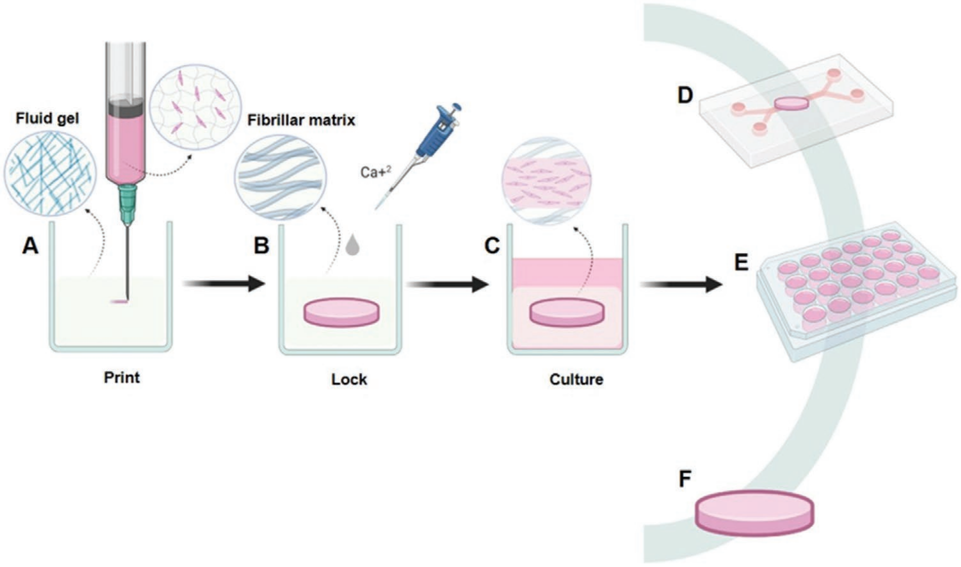

Figure 1. The print-then-lock concept for the fabrication of bioprinted microphysiological systems embedded within a bioinspired hierarchical fibrillar matrix. A) Colloidal suspensions of CNC with defined rheology are used as support fluid gels to fabricate 3D constructs with arbitrary geometries. B) The printed constructs are then locked within a fibrillar matrix by inducing CNC self-assembly with the addition of calcium ions. C) Bioprinted constructs embedded within the fibrillar matrix are cultured for in vitro maturation and bioassays. This platform enables possible application as: D) housing support materials for tissue and organ-on-chip microfluidic device; E) on-plate 3D bioprinted models for medium- to high-throughput assay replicates; F) temporary templating bioreactors for in vitro maturation of 3D bioprinted tissue constructs that can be harvested after CNC matrix bioorthogonal digestion.

mechanotransduction, or morphogenesis.[8,12] In addition to biophysical cues, the permeability allowed by the interstitial space of fibrous ECMs is also crucial for regulating cell signaling because it controls the permeation and mass transport of bioactive macromolecules, nutrients, and wastes.[13]

Although numerous pathophysiological findings have derived from OoC models housed in the typical plastic platforms commonly used for microfluidic device fabrication, their inability to recreate the 3D fibrillar nature of the compartmentalization barriers and the interstitial spaces where biological processes occur is a major limitation of these systems.[14] Moreover, tissues and organs have 3D structures with architectures on different length scales crucial for their complex biological function,[15] which are difficult to reproduce on current OoC platforms usually based on circuits with fixed predefined geometries.[16] Additionally, many conventional microfluidic devices often require cumbersome microfabrication manufacturing processes[17,18] and complicated cell and biomaterial handling procedures that have not yet proven to be sufficiently efficient, feasible, or economical.[19] Therefore, combinations of fabrication strategies and biomaterial platforms enabling the automated manufacture of 3D cellular constructions while providing the intrinsic barrier function of fibrillar ECMs and BMs would be a major advance in the field. By allowing the creation of OoC systems with more biomimetic cell–cell and cell–matrix crosstalk, such a platform would contribute to the construction of complex compartmentalized 3D tissue models with higher physiological relevance.

Self-assembling materials, of either natural or synthetic origin, offer unique advantages to provide a rich landscape of ECM-mimetic nanoscale filamentous structures, networks, and pores.[16] If rationally integrated with biofabrication technologies such as 3D bioprinting,[1,20] these man-made supramolecular hydrogels can be leveraged for the bottom-up assembly of complex 3D structures with well-defined nano-to-macroscale hierarchical architectures. A few recent studies have started to explore this biofabrication approach. For example, fibrillar bioinks based on ultrashort peptide self-assembly were applied to print stable large-scale constructs with high shape fidelity, enabling long-term cell survival and robust chondrogenic differentiation of mesenchymal stem cells.[21] The Mata research group has been exploring the interfacial coassembly between elastin-like recombinamer and graphene oxide for the liquid-in-liquid bioprinting of perfusable fluidic devices with nanostructured wall membranes showing tunable anisotropic permeability.[22,23]

Building on these concepts, here we propose an innovative bottom-up strategy for the direct manufacture of cell-laden devices that recreate the unique biophysical cues from the native fibrillar ECMs while allowing the design of embedded bioengineered constructs with arbitrary geometries. The proposed platform combines the concepts of 3D free-form bioprinting in suspension media[24] with the controlled self-assembly of plant-derived cellulose nanocrystals (CNC)[8,25] as building blocks to fabricate cell-laden constructs embedded within its own fibrillar hydrogel device (**Figure 1**). An inherent requirement of the proposed hypothesis is that hydrogel formation has to occur around cells and therefore fiber assembly and gelation mechanisms have to be cytocompatible. The ability to regulate the rheological behavior of CNC colloidal suspensions and induce their ion-mediated self-assembly by nanoparticle surface charge screening with biocompatible ions[26] suggests that it might be a well-suited option for the implementation of this fabrication strategy. However, fine control over such mechanisms, not only to produce a fluid gel with the required rheological behavior to assist on the bioprinting process[24] but also to lock the resulting structures within a stable fibrillar matrix after printing, need to be optimized. A few examples of granular microgels[27,28] or shear-thinning macromolecular hydrogels systems based on specific chemical modifications for reversible crosslinking[29] have been proposed as support materials for the direct writing and long term maturation of embedded 3D cellular constructs, as well as to support the bioassembly of cell spheroids.[30] Although these systems could be considered as alternatives to implementing the concept proposed here, they do not recapitulate the filamentous nature of the ECM, among other comparative disadvantages to CNC-based fibrillar matrix in terms of synthesis complexity and cost of implementation. On the other hand, fibrillar proteins, such as fibrin or collagen, could be considered as an alternative to CNC to implement this strategy. However, although it has been shown that fibrin gels could retain cell spheroids in defined positions of the 3D space placed by a custom-made printing system and then assist on their bioassembly during culture,[31] fibrin and collagen gels do not show the required shear-thinning and self-healing behavior to be used as support baths for the bioprinting of complex 3D structures using the traditional extrusion-based systems. Moreover, unlike CNC that are low cost xeno-free materials, these proteins are usually obtained from animal origins, result in soft gels with low capacity to retain the original shape of 3D printed structures and undergo cell-mediated retraction, suffering as well of fast proteolytic degradation during in vitro cell culture.[32,33] These characteristics limit their potential to be used as housing material for dynamic in vitro modeling, particularly if medium to long-term cell culture is aimed.

To test the versatility of the proposed platform, here we produced CNC fluid gels with optimized rheological properties meeting the demands for 3D bioprinting in suspension media and controlled its further self-assembly into fibrillary hydrogel devices after printing the desired complex 3D structures. The combination of these hierarchical support material and fabrication technology for creating microfluidic channels and multicellular 3D constructs embedded within a biomimetic fibrillar matrix is demonstrated, facilitating the rapid generation of large numbers of microphysiological systems that can be leveraged for in vitro modeling in different assay formats. The implementation of the proposed concept is tested with various cell types and bioinks, and their biological performance is evaluated in both static and dynamic conditions. The range of comparative advantages offered by this system further provides a potential solution to scale-up for bioengineered tissue manufacture.

2. Results and Discussion

2.1. Self-Assembled CNC Fibrillar Hydrogels as Support Matrix to "print-then-lock" Embedded Structures

A key requirement to enable the printing of high-resolution constructions applying the strategy of 3D bioprinting in suspension media is the use of support baths with adequate rheological behavior capable of providing a semisolid medium to print into.[24] CNC colloidal stability in aqueous media depends on its synthesis method but is often based on electrostatic repulsions provided by surface-charged groups.[25,34] On the other hand, due to their abundant surface hydroxyl groups, CNC can establish extensive hydrogen bonding and form shear-thinning physical gels at high nanoparticle concentration (usually above ≈7 wt%),[35] suggesting that it can potentially be used as a fluid gel to assist bioprinting processes. Interestingly, shielding of CNC surface charges with mono or bivalent biocompatible ions (e.g., Na^+ or Ca^{2+}) has been applied not only to control the rheological behavior of these colloidal suspensions and produce viscous gels at much lower nanoparticle concentration (lower limit of about 1 wt%) but also to induce the further self-assembly of these building-blocks into bioinspired fibrillar hydrogels with high structural cohesion and optical transparency.[26,36] These intrinsic properties of CNC suspensions are thus fundamental for the concept here proposed because they can be explored to produce fluid gels as support baths for high-resolution printing of complex compartmentalized 3D freeform structures, as well as for its further embedding within a biomimetic ECM fibrillar matrix under straightforward biocompatible conditions, a concept that we term as "print-then-lock" approach.

To prove this, CNC were produced from microcrystalline cellulose by sulfuric acid hydrolysis, a method that leads to negatively charged nanoparticles grafted with sulfate groups on their surface.[37] Their morphological characterization by scan transmission electron microscopy (STEM) showed rod-shaped nanocrystals with the dimension of 173.4 ± 16.1 nm in length and 4.9 ± 1.8 nm in width (**Figure 2B**), consistent with our previous studies.[38,39] The viscoelastic behavior of CNC suspensions as a function of nanoparticle and calcium ions concentration was then characterized. To establish the window of CNC versus ionic strength that leads to fluid gels displaying suitable behavior to assist the printing process, we first performed a qualitative evaluation by a simple inversion test (Figure S1 Supporting Information). The range of tested CNC and Ca^{2+} concentrations was selected to vary around the reported threshold values for CNC sol–gel transition by addition of this ion,[27] which are situated at ≈1.5 wt% and $\approx 2.0 \times 10^{-3}$ м, respectively. Results show that the viscosity of CNC suspensions has a mutual nanoparticle—ionic strength dependence: they start to become viscous enough to resist gravity-driven flow at CNC concentrations of 1.5 wt% with the addition of 2.5×10^{-3} м of Ca^{2+} and resulted in viscous gels that did not flow (within the time frame of the test) at 2.5 wt% CNC and 2×10^{-3} м Ca^{2+}. To evaluate if these gels could be applied as support media to assist in the embedded bioprinting process, preliminary printability tests were performed using a 10 wt% gelatin ink. As seen in Figure S2A in the Supporting Information, the lower limit of parameters that ensured printability is 2 wt% CNC and 1.5×10^{-3} м Ca^{2+}. While keeping the CNC concentration constant at 2.5 wt% and varying the ionic strength of the suspension ($1.5–7.5 \times 10^{-3}$ м Ca^{2+}), 2×10^{-3} м Ca^{2+} fluid gel showed the best performance in retaining the printed structure's shape and fidelity (grid pattern, 20% infill, 27G needle as a nozzle) without leaving noticeable crevices and raised peaks in the CNC support matrix originated by the movement of the nozzle, which in contrast could be well noticed in the 7.5×10^{-3} м Ca^{2+} formulation. Rheology tests were then performed to further assess the impact of ionic strength on the viscoelastic behavior of CNC suspensions and confirmed that they exhibit the required properties

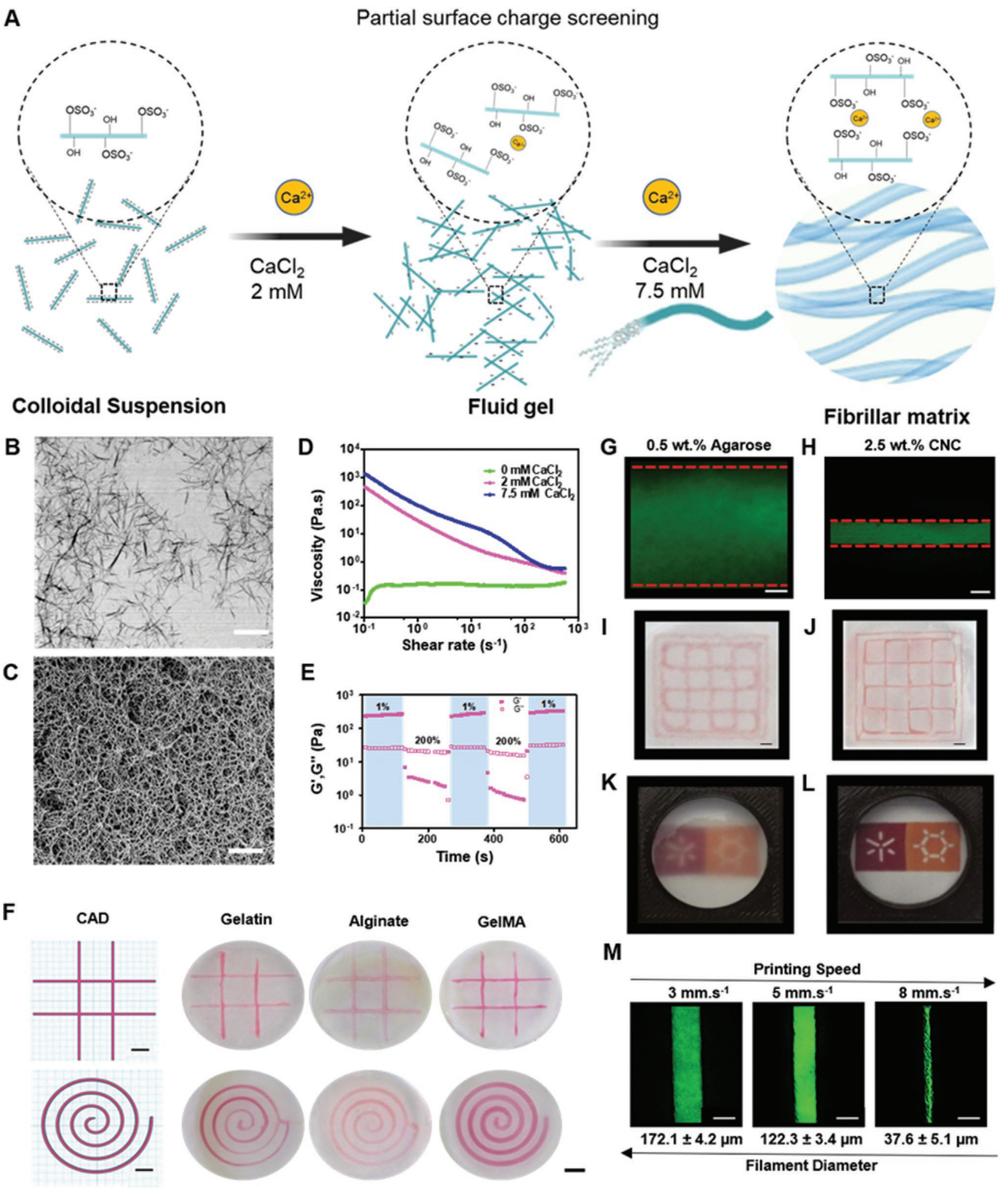

Figure 2. A) Schematic illustration of the transition of a colloidal suspension of CNC into a fluid gel by partial surface charge screening on the addition of Ca^{2+} ions followed by its locking into fibrillar matrix by CNC self-assembly induced by the addition of excess cations. Scanning electron microscopy images (SEM) of B) CNC showing its rod-shaped morphology, and C) self-assembled hydrogel showing hierarchical arrangements of CNC into fibrillar networks (scale bar: 200 nm). D) Shear viscosity of the 2.5 wt% CNC suspensions at variable concentration of Ca^{2+} ions: 0×10^{-3} M (green), 2.5×10^{-3} M (pink) and 7.5×10^{-3} M (blue). E) Evaluation of self-healing properties CNC hydrogel by subjecting the 2.5 wt% CNC with 2×10^{-3} M Ca^{2+} (pink) or 7.5×10^{-3} M Ca^{2+} (blue) to alternating high (200%) and low (1%) strain cycles (G': storage modulus, solid symbols, G'': loss modulus, hollow symbols).

to be used as a support media for embedded bioprinting. The shear rate dependence of viscosity of 2.5 wt% CNC suspensions at different electrolyte concentrations are shown in Figure 2C and its corresponding strain sweeps are shown in Figure S2B (Supporting Information). In agreement with the results of the qualitative assays, increasing Ca^{2+} gradually increased the viscosity of the CNC suspensions as a result of nanoparticle surface charge screening, which compresses the thickness of the electrical double layer and promotes their lateral aggregation.[40] During this process, CNC established enough network percolation,[26] transitioning from low viscosity liquids to solid-like hydrogels of increasing storage moduli following the increase of suspension's ionic strength (Figure 2A). These results are in good agreement with previous studies where the dependence of CNC hydrogel stiffness on ionic strength has been demonstrated, a phenomenon attributed to enhanced side-by-side self-assembly of CNC promoted by the effects of cations addition.[26,41] Mechanistically, the addition of Ca^{2+} ions reduces the Debye length of nanoparticles that consequently leads to their lateral aggregation driven by dominant attractive interactions (e.g., van der Waals forces and hydrogen bonding) mainly established by the abundant hydroxyl groups on their surface. When CNC fluid gels were locked with an excess of Ca^{2+} (7.5×10^{-3} M), it resulted in stable hydrogels with a well-developed hierarchical fibrillar architecture, as shown in Figure 2C. Interestingly, it has been previously suggested that divalent cations whose metal sulfates have low solubility in water such as the Ca^{2+} used here, can more effectively bridge two sulfate groups of adjacent CNC, imparting an interparticle crosslink effect to the system that leads to more stable and rigid hydrogels that those produced with Mg^{2+} or monovalent ions such as Na^{+}.[27] Remarkably, this man-made biomimetic matrix was composed of entangled fibrils with a mean diameter of 28.5 ± 11.3 nm and mean pore size of 76.7 ± 17.8 nm (Figure S2F,G, Supporting Information), falling within the corresponding range of dimensions found in native ECMs.[8,10,11] In vivo, the ECM fibrils of parenchyma and stromal tissues varied from 10 nm to 230 nm, depending on the tissue type,[8] while the dense 3D networks of BM had a pore size ranging from about 10 to 130 nm.[10,11]

Of particular interest for the proposed application was the CNC fluid gel shear-thinning (Figure 2D) and stress-yielding (Figure 2E) responses, reflecting the shear-induced disruption of the non-covalent nanoparticle assemblies formed by the addition of Ca^{2+}. Moreover, after disruption by an external mechanical stimulus, CNC hydrogels were able to rapidly recover from a predominantly viscous to a predominantly elastic state (Figure 2E), demonstrating self-healing potential.[42] Interestingly, similar self-healing behavior has also been observed in CNC hydrogels produced by hydrothermal desulfation of their surface.[43] This suggests that the multiple non-covalent interactions established between the high surface area and aspect ratio CNC, including not only van der Waals and hydrogen bonding but likely, also ionic bridging mediated by Ca^{2+}, are main contributors for the observed self-healing behavior of CNC fluid gels. This characteristic is essential as support media in order to hold in place the extruded ink behind the nozzle after printing and prevent crevice formation.[44] The tunable rheology of CNC suspensions mediated by Ca^{2+} ions confers to this material excellent properties as a support media for printing with different inks, including liquid build constructions based on different post-printing solidification approaches.[44] In fact, 3D printing with liquid and low viscosity inks is still the main challenge in extrusion-based bioprinting, limiting the options of biomaterials and crosslinking mechanisms that can be used with these technologies.[45,46] To illustrate the freedom of biomaterial choice allowed by our CNC-based fluid gel we printed various low viscosity inks based on hydrogel precursors with different crosslinking mechanisms (Figure 2F): 5 wt% gelatin crosslinked by microbial transglutaminase (mTG)[37,47] diffusing from CNC fluid gel as representative of enzymatic crosslinking (GelTG), 2 wt% alginate as representative of ionic crosslinking, and 5 wt% methacrylated gelatin (GelMA) as representative of photo-crosslinking. Based on the results of the rheological characterization, 2.5 wt% CNC suspensions with 2×10^{-3} M Ca^{2+} were selected as support fluid gel to assist the printing process and a 7.5×10^{-3} M Ca^{2+} solution was used to induce the post-printing self-assembly of CNC, embedding the printed structures within the fibrillary matrix according to the proposed "print-then-lock" concept. As shown in Figure 2F, the resolution and fidelity of the printed patterns were well maintained, irrespective of the nature of the ink polymer or its crosslinking mechanism. This versatility is not only particularly interesting for the proposed concept, but also for the field of embedded bioprinting in general as it confers low restriction on the type of ink material that can be explored for each particular application.

Besides the advantages of versatility in ink choice, the CNC fluid gel also provided improved printing fidelity and resolution compared to other microparticle-based support materials typically used in the field. To demonstrate its superior performance in assisting the printing process, we compared CNC with an agarose microparticle fluid gel that has been widely used as a support bath in several studies,[48,49] including our own.[50] As shown in Figure 2G,H, 5 wt% gelatin ink printed at the same speed and pressure with a 27G nozzle into these two different support materials result in filaments with diameters of 904.6 ± 34.1 μm in the agarose bath (Figure 2G) and of 181.2 ± 11.3 μm in our CNC fluid gel (Figure 2H). Further, while the irregular agarose microparticles created tortuosity on the print bed path that leads to roughened filaments with a variable diameter[48] (Figure 2I), a problem shared by the other microparticle-based support materials,[51] no major visible distortion or particle footprints were seen on the surface of the filaments printed in

F) CAD design and respective photographs of two-layered linear patterns and a continuously extruded spiral printed in CNC colloidal matrix with 5 wt% gelatin (GelTG, enzymatic crosslinking), 2 wt% alginate (ionic-crosslinking) and 5 wt% GelMA (photo-crosslinking) (scale bar: 500 μm). Confocal images comparing the resolution of fluorescently labeled (FITC) gelatin ink printed within G) 0.5 wt% agarose slurry and H) 2.5 wt% CNC colloidal suspension (scale bar: 250 μm). Photographs of lattice structures with 10 × 10 × 1 mm and 20% rectilinear infill printed in I) 0.5 wt% agarose slurry and J) 2.5 wt% CNC colloidal suspension (scale bar:1 mm). Photographs showing the optical transparency of K) agarose bath, and L) CNC colloidal suspension. M) Resolution of FITC-labeled gelatin 5 wt% ink printed at a constant pressure of 5 kPa and variable speed of 3, 5, and 8 mm s^{-1} with a 30G nozzle (scale bar: 150 μm). Images are representative of $n = 3$ independent experiments, data are means ± SD.

our colloidal CNC fluid gel (Figure 2J). Due to the rapid self-healing behavior of this support material, the filament resolution could be easily tuned by varying the printing speed without negatively affecting the dispersion and distribution of the ink, ranging from 172 ± 4.2 µm at 3 mm s^{-1} down to 37 ± 5.1 µm at 8 mm s^{-1} (Figure 2M, Figure S3A,B Supporting Information). Similarly, unlike microparticulate baths[48,51] that are typically translucent but not completely transparent compromising its macro and microscopic post-printing optical analysis (Figure 2K, Figure S3C, Supporting Information), our fibrillar CNC matrix is highly transparent (Figure 2L, Figure S3D, Supporting Information).

Next, we tested the capability of the CNC fibrillar matrix to withhold perfusable channels, an integral feature of microphysiological systems built on microfluidic OoC platforms.[52] The thermoresponsive polymer Pluronic F-127 was used as fugitive ink to create an open channel (**Figure 3A**). After printing the desired structures (Figure 3B) and locking the CNC with calcium ions (Figure 3C), the perfusability of the created channels was demonstrated by injection of colored dye solutions (Figure 3D, Movie S2, Supporting Information). To show that perfusable microchannels can be easily fabricated in our "print-then-lock" system irrespective of their design complexity, we printed a series of structures with different arbitrary patterns: a common microfluidics chip design with bifurcated channels (Figure 3E), a design with three different inlets and a convergence point in the middle (Figure 3F), and multilayered channels (Figure 3G). The capacity for automated fabrication of perfusable microchannel networks with structural integrity using this system shows that it can be considered as an alternative to conventional polymeric microfluidic chip platforms,[7] with the advantage of allowing the direct 3D writing of heterogeneous microphysiological systems requiring compartmentalization and perfusion for in vitro tissue/organ and disease modeling. Furthermore, these fabrication steps can be performed under biocompatible conditions, an aspect that has several advantages over competing technologies, beyond the inherent benefits derived from its potential to emulate the physical cues of the ECM fibrillar structure. For instance, compared to other nanocellulose-based paper devices fabricated applying similar matrix-assisted 3D printing concepts, it avoids the need for post-printing construct drying to confer structural cohesion to the device or the need for high-temperature treatments and extensive organic solvent washing for the removal of hydrophobic sacrificial inks.[53,54] On the other hand, compared to PDMS-based microfluidic devices, the most popular platform used in the field, it bypasses the need for multiple and tedious microfabrication steps required for their manufacturing.[55,56] Moreover, CNC are derived from renewable plant-based sources providing a green chemistry and sustainable alternative to existing plastic polymers widely in use for fabricating microfluidic devices.[57]

A fundamental requirement for developing functional in vitro tissue models is ensuring the availability of oxygen, nutrients, and signaling molecules to support cell activities. Thus, controlling their diffusion and permeability through cellular constructs is a key factor to be addressed while developing these systems.[58] As discussed above, BM and ECM play critical roles in the regulation of this mass transport phenomena, which are essential for cell function but are poorly recreated by the solid polymeric materials and microporous membranes used as barriers for cellular compartmentalization in microfluidic devices.[3] The fibrillar nature of the CNC matrix suggests that it can better mimic the interstitial permeability of the ECM for biomolecule diffusion, contributing to improving the biological relevance of the fabricated microphysiological systems in comparison with polymeric barriers used on OoC devices. To demonstrate the permeability of the CNC matrix for biomolecules of different sizes, we evaluated the diffusion of FITC-labeled dextrans (4 kDa and 250 kDa, used as model biomolecules) through the fibrillar network from a sacrificially printed 200 µm microchannel over the time course of 60 min. Although the low molecular weight dextran (Figure 3H–J) logically diffuses faster than the corresponding high molecular weight (Figure 3K–M), the interstitial porosity of the CNC matrix (Figure S4, Supporting Information) allows an easy but controlled spatiotemporal diffusion of biomolecules, creating concentration gradients through the hydrogel volume. This permeability is in different aspects remarkable for support and barrier materials of microphysiological systems. First, it ensures that the compartmentalized 3D cellular constructs embedded in the matrix will receive the nutrients they need to survive while allowing cellular signaling crosstalk during the in vitro maturation and functional assessment steps. Second, by generating concentration gradients of biomolecules, which play key roles in the regulation of a wide range of biological processes including, e.g., development, wound healing, or cancer metastasis,[59] it will improve the biological significance of the proposed models compared with the typical mass transport occurring through perforated membranes used in microfluidic OoC devices.

On the other hand, the 3D shape and architecture of cellular constructions are known to significantly affect the functional outcome of bioengineered tissue/organ in vitro models.[60,61] Therefore, the ability to precisely recreate the specific 3D architectural hallmarks of each tissue contributes to increasing the predictive power of these bioengineered systems.[3] The concept of bioprinting complex heterogeneous models embedded within its own support bioreactor is largely dependent on the properties of the fluid support media. The overall goal of the strategy is to achieve multi-component and multilayered structures without dispersion of extruded bioinks while maintaining the structural fidelity of the construct. Applications of 3D printing in support media have used different granular,[49,62] microparticle[48,51,63,64] or even liquid solution[65] as fluid supporting material. Despite the significant advances, a compromise between either shape fidelity and resolution or biocompatibility and biomimicry along with, in some cases, the need for extensive processing[53] have been often required. To demonstrate the capability of our CNC fluid gel to support the easy fabrication of delicate freeform structures using low viscosity inks, we printed a 15 mm high multicomponent coil using GelTG and multiple printheads.[49] As shown in Figure 3N–O, the CNC matrix allowed high-resolution printing of the coil, without noticeable distortions caused by the repeated movements of the nozzle in 3D space during the printing process. Moreover, our system also enables the relatively fast fabrication of dense volumetric structures with excellent resolution and precision,

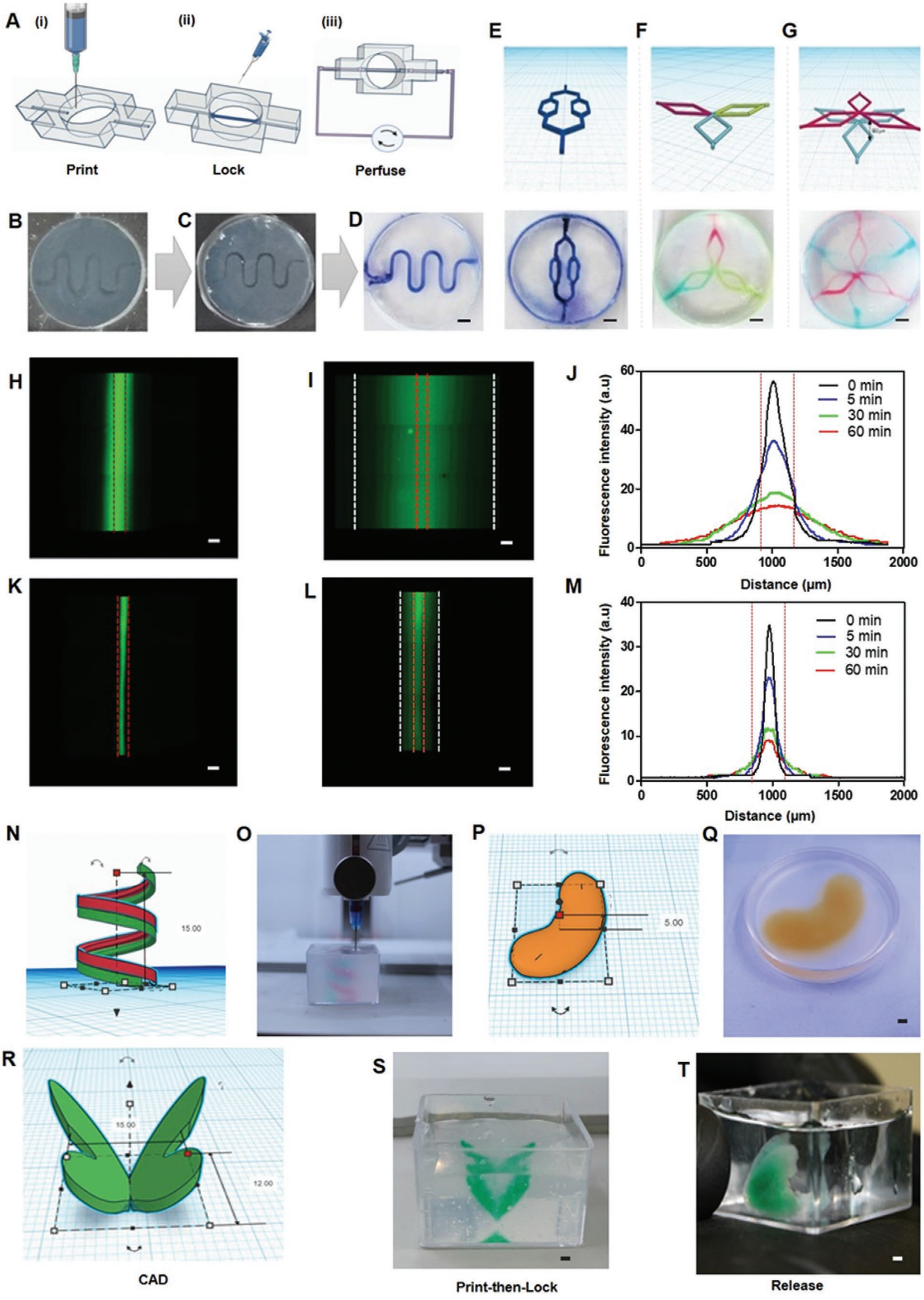
A
(i)
(ii)
(iii)
Print
Lock
Perfuse
E
F
G
B
C
D
H
I
J
Fluorescence intensity (a.u)
0
20
40
60
0 min
5 min
30 min
60 min
0
500
1000
1500
2000
Distance (μm)
K
L
M
Fluorescence intensity (a.u)
0
10
20
30
40
0 min
5 min
30 min
60 min
0
500
1000
1500
2000
Distance (μm)
N
15.00
O
P
5.00
Q
R
15.00
12.00
CAD
S
Print-then-Lock
T
Release

as demonstrated by the printing of a miniaturized right human kidney (5 mm height, 25 layers, and 65% infill, printing time = 7 min, Figure 3P,Q). Note that extrusion-based bioprinting is slower than other emerging stereolithography-based methods for bioprinting of complex structures, although currently they still possess lower potential for multicellular construction.[66,67]

Interestingly, nanocelluloses are biocompatible materials that are not biodegradable in mammalian organisms but can be bioorthogonally degraded by cellulase enzymes (the resulting by-product being just glucose).[25,68] Thus, the CNC matrix can be used as a template bioreactor for the in vitro maturation of complex bioprinted constructs and then allow their mild release by enzymatic digestion of the support material for downstream in vitro biological analysis or even for its potential in vivo transplantation. To demonstrate this, we printed a complex 3D butterfly of 15 mm height, 12 mm width, and variable wing thickness ranging from 1.5 mm at the bottom down to 0.5 mm on top with GelTG ink (CAD design in Figure 3R, Movie S1, Supporting Information). After printing, the structure was locked in the CNC matrix by addition of calcium ions (Figure 3S), allowed to crosslink for 30 min and then released from the support materials by digestion of CNC with cellulase under cell culture conditions (cell culture media at 37 °C for 24 h).[68] Unlike mechanical aspiration of the granular and microparticles based slurries typically used as support baths,[69] a process that can jeopardize the integrity of delicate structures, the enzymatic release is slower but leaves no major visible residues of the support material on the released structure and the fidelity of the 3D printed model was well preserved (Figure 3T), as previously shown using enzymatic degradation of alginate microparticles.[63]

2.2. Manufacturing Microphysiological Systems Embedded into CNC Fibrillar Matrix

Next, we evaluated the performance of the CNC matrix as a platform for building living microphysiological systems. To demonstrate that it can support the bioprinting of complex 3D structures and their long-term in vitro maturation, we tested different low viscosity bioinks and used human adipose-derived stem cells (hASCs) as a representative source of stromal/stem cells widely applied on the fabrication of tissue-engineered constructs.[70] Although more challenging to print,[71] bioinks with relatively high cell densities (6×10^6 cells mL^{-1}) were chosen due to the increasing evidence that cell–cell interactions are essential for their condensation into functional bioengineered tissues[72,73] and therefore might contribute to improve the biological significance of fabricated systems. Two different hydrogel precursors were tested: gelatin (5 wt%, GelTG), a widely used bioink material;[71] and platelet lysate (PL), a bioactive human-derived liquid formulation that, as we have recently demonstrated,[50] gels in the presence of calcium ions, promotes fast cellular colonization and remodeling of bioprinted constructs, but lacks the physical properties to maintain its structural integrity.

Filaments showing good resolution and homogenous cell distribution without noticeable dispersion into the support material were obtained with both bioinks (**Figure 4A**,B, Figure S5A,B, Supporting Information). This confirms that the CNC fluid gel provided the required flow restriction for the extruded solutions, and its further self-assembly into a fibrillar matrix by Ca^{2+} ions locks the printed structures in space during bioink gelation. Moreover, the CNC matrix supported the in vitro maturation of embedded 3D printed constructs, maintaining high cell viability (Figure 4D,E) and the original filament shape resolution (Figure 4C). Interestingly, although no significant difference was observed in cell density at day 1, PL-based bioink showed a twofold increase in cell density compared to gelatin at day 14 (Figure 4F), demonstrating its highly inductive cell proliferation properties.[33] The high cell density, viability, and shape fidelity are not only maintained in simple constructs with low infill but also in complex volumetric 3D bioprinted structures (miniaturized structure of human femur bone, 60% infill, Figure 4G–I). This combination of PL-based bioink and support device might therefore be an interesting fabrication option to reduce the time required to generate mature 3D constructs with organotypic cellular density, as preferred for improving functional in vitro modeling.[3,74]

To demonstrate that the maturated tissue can be harvested from the support materials on-demand after the culture steps, disc-shaped constructs (rectilinear pattern, 25% infill, 27G nozzle) were printed with GelTG, cultured within the CNC fibrillar matrix for 7 days, and then retrieved via enzymatic hydrolysis with cellulase.[68,75] As shown in Figure 4J–M, the densely cellularized construct kept its 3D printed shape and

Figure 3. A) Illustration of the process for direct 3D printing perfusable channels within CNC fibrillar matrix: i) print channel circuit with fugitive ink, ii) lock structure inducing self-assembly of the CNC with Ca^{2+}, (iii) perfusion of the self-standing embedded channel after purging the sacrificial ink. B) Photograph of a printed and locked sinusoidal filament with Pluronic F-127 fugitive ink, C) its liquefacation at 4 °C, and D) perfusion of the hollow channel with water (added food color for visualization). CAD models and respective perfusion of resulting microfluidic chip with E) bifurcated design, F) independent inlets and bifurcations with common convergence point (water with different food colors is perfused to aid the visualization of each channel independently), G) multilayered channels separated by a depth distance of 500 µm (water is perfused with blue food color in the bottom layer and red in the top layer to aid visualization, scale bars in B, C, D, E, F, G: 1 mm). Time-lapse fluorescence images of a hollow channel filled with dextran 4 kDa at H) 0 min and at I) 60 min postinjection. J) Plot of spatiotemporal fluorescence intensity for dextran 4 kDa throughout CNC matrix. Time-lapse fluorescence images of a hollow channel filled with dextran 250 kDa at K) 0 min and at L) 60 min postinjection. M) Plot of spatiotemporal fluorescence intensity for dextran 250 kDa throughout CNC matrix. Red and white dotted lines represent the limits of the fabricated channel and of detected fluorescence, respectively (scale bars in H, I, K, L: 200 µm). N) CAD model of the suspended spiral with 15 mm height, and O) respective embedded 3D print with multiple printheads. P) CAD model of miniaturized human right kidney, and Q) respective 3D printed structure with high volumetric infill (65% concentric infill pattern, 25 layers with 200 µm layer height). R) CAD model of a butterfly, and S) respective 3D printed and locked structure (height 15 mm and width 12 mm, wings with 1.5 mm thickness on the bottom and 0.5 mm on top). T) Released structure immersed in PBS after enzymatic hydrolysis of CNC matrix with cellulase. O, Q, S structures were fabricated using GelTG ink and 27G nozzle. Food colors were added to aid visualization, (scale bars in Q, S, T: 1 mm).

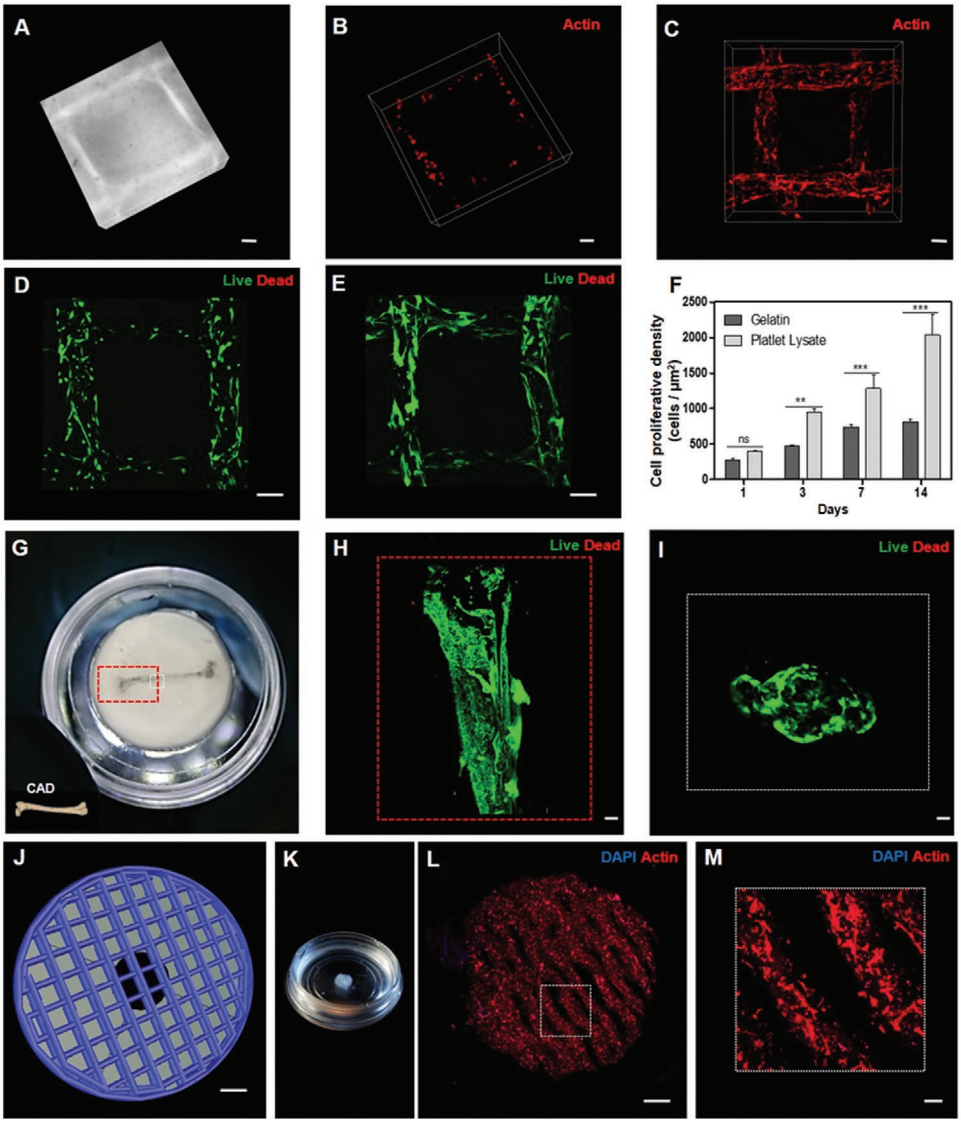

Figure 4. A) 3D brightfield image reconstruction of CNC matrix embedding lattice structures printed with hASCs in PL bioinks (rectilinear pattern, 25% infill printed with 27G nozzle), and B) respective confocal laser microscopy (CLM) image sowing hASCs spatial distribution at day 0. C) 3D CLM image of hASCs cytoskeleton in PL bioinks after 4 weeks in culture. (A, B, C scale bar: 200 µm). hASCs viability (live\dead assay) in bioprinted constructs with D) GelTG; and E) PL hydrogel bioinks after 14 d of culture (D, E scale bar: 200 µm). F) Estimation of cell proliferation based on cell density by construct areas over a culture period of 14 d (ns $p > 0.05$, * $p < 0.01$, ** $p < 0.001$, *** $p < 0.001$, determined by two-way ANOVA followed by Tukey's post hoc tests). G) CAD design of miniaturized human femur along with a photograph of the respective embedded bioprinted construct using hASCs in PL bioink after 2 weeks of culture. H) CLM projection image of live\dead assay of the biofabricated femur embedded in CNC fibrillar matrix and I) its cross-section cut view (H and I scale bar: 1 mm). J) CAD design of 3D disc model with 5 mm diameter and 1 mm height. K) Photograph of the enzymatically (cellulose) released bioprinted disc-shaped construct after 7 d in culture, and L,M) its respective CLM images of cell cytoskeleton (scale bar *L*: 1 mm, *M*: 100 µm). Images are representative of $n = 3$ independent experiments, data are means ± SD.

microfilament resolution after release, demonstrating that the reverse templating process is stable and effective.

While different strategies for manufacturing microphysiological systems have been tested, yielding excellent results, they often have limitations of scalability or adaptability required for in vitro applications.[76] Most of the current complex tissue chip platforms are of very low throughput, allowing up to dozens of replicates to be performed simultaneously, in the best-case scenarios.[5] As they improve throughput capacity, tissue plate platforms (arrays of tissue chips for on-plate replicates) are becoming popular options for in vitro modeling.[7] However, although addressing the question of sample replicates, these platforms are based on predefined sample housing circuits, sacrificing the flexibility and adaptation of the chip configurations for specific biological contexts of use. Therefore, automated biofabrication platforms that contribute to facilitating the manufacture of miniaturized OoC systems at higher throughputs and replication numbers are highly sought in the field.[77,78] Our CNC platform allows the rapid generation of large numbers of highly reproducible heterogeneous constructs with arbitrary

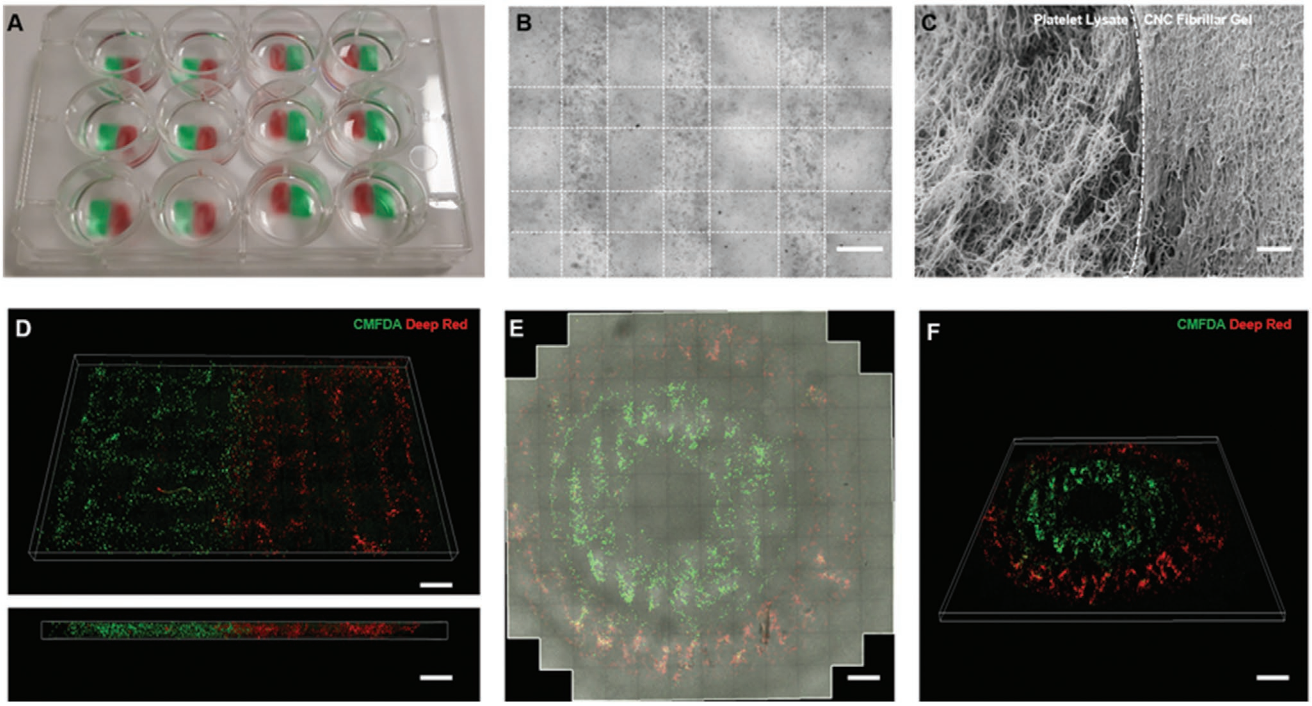

Figure 5. A) Photograph of representative heterogeneous tissue model with the dimension of 10 × 10 × 0.4 mm and 200 µm layer height (2 layers) printed in a 12-well tissue culture plate (food colors were added into the ink to aid on visualization). B) Transmitted light microscopy image of embedded constructs printed with hASCs in PL bioinks, showing the transparency of the CNC fibrillar matrix enabling real-time optical analysis (scale bar 250 µm). C) SEM image from the cross-section of the interface between PL embedded within the fibrillar matrix of CNC (scale bar 500 nm). D) 3D reconstructions of CLM images of the heterogonous model of tissue interface, where hASCs were labeled with green or red cell tracker and bioink hydrogels used are PL or GelTG, respectively (scale bar: 1 mm). E) Bright-field and CLM tile scan image of heterogeneous circular construct embedded within the CNC matrix illustrating cell compartmentalization, along with F) the respective 3D reconstruction of this CLM image (scale bar: 1 mm).

and fast and easy to redesign 3D shapes on standard cell culture multiwell plates (**Figure 5A**). For instance, it took less than 5 min to print 12 replicates of a two-component squared structure with dimensions of 10 × 10 × 0.4 mm and 20% rectilinear infill pattern with a 27G nozzle, allowing immediate real-time monitoring of embedded cell patterns without compromising the integrity of fabricated constructs (Figure 5B). Furthermore, it enables the manufacturing of multicellular and multicomponent 3D systems with cell compartmentalization within an ECM mimetic fibrillar matrix (Figure 5C), or the simulation of tissue interfaces typically found in most OoC platforms.[3] As shown in Figure 5D–F using hASCs labeled with a fluorescent dye and encapsulated in different bioink hydrogels (PL and GelTG) for demonstration, heterogeneous 3D constructs with different geometries and microscale precision could be easily printed without requiring specialized expertise for the fabrication or operation of the device. These represent comparative advantages over the time-consuming steps of microfabrication (in the order of days) and cell loading required to build microphysiological systems on customized PDMS-based platforms.[79]

2.3. Fabrication of Dynamic OoC Systems Enabled by Multimaterial Bioprinting Approaches

Besides recreating the 3D nature and arrangements of tissues integrating multiple cell types to reflect its physiological context, a key feature of OoC models are the biochemical and biophysical cues deriving from the emulation of their dynamic environments. One way of adding dynamic environmental factors in these models is by introducing fluid flow across tissues through microfluidic channels or bioengineered vasculature, to deliver and remove cell culture media and also to remove associated cell metabolites and wastes.[3] In the simplest approach, tissue plates use gravity-driven flow to perfuse the system, eliminating the need for use of external pumps and maintaining the advantages of well plate format.[7] Considering that the CNC platform allows the printing of dense volumetric structures, it should allow the incorporation of sacrificial reservoirs and fluid circuits for similar gravity-driven flow systems. However, certain applications might require a finer fluid flow control that can only be provided by external pumps. Therefore, we explored the potential of multimaterial biofabrication approaches to manufacture microphysiological systems incorporating different types of cells within its own microfluidic perfusion bioreactor.

We started by engineering vascular channels, a key component of many tissue interface models. Silicone gaskets were first printed on a glass slide demarcating the outer border of the 3D tissue chip that was then filled with CNC fluid gel (**Figure 6A**). Next, instead of using fugitive inks to create open channels requiring subsequent cell lining, HUVEC suspended in gelatin was used as bioink for direct printing the vascular channel and simultaneously achieve its in situ endothelization.[80,81] After printing, the channel structure was connected to hollow

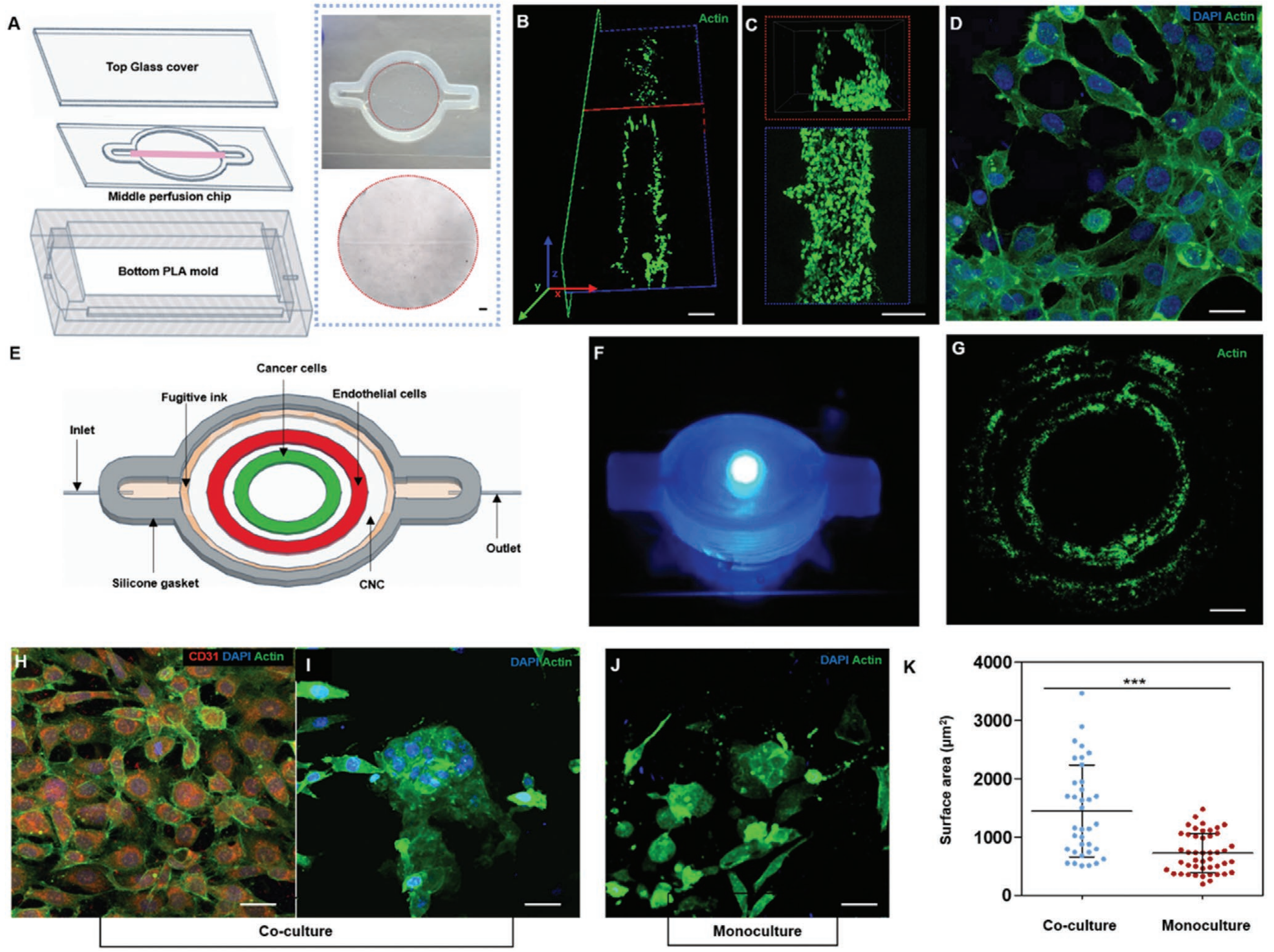

Figure 6. A) Schematic of the assembly of 3D bioprinted chips on printed polylactic acid (PLA) supports used for chip sealing and perfusion (left), and a photograph of 3D printed chip made of silicone gasket filled with CNC where HUVEC suspended in gelatin where bioprinted, scale bar: 500 µm (right). B) 3D reconstruction CLM images of HUVEC cytoskeleton (green) and nuclei (blue) within bioprinted channels where cells organize into a tubular monolayer after 2 weeks under constant perfusion (scale bar: 200 µm). C) Magnified projection image of the channel in B, along with 3D cross-section view of endothelialized channel showing an open lumen (scale bar: 100 µm). D) Higher magnification image of B showing endothelial cell monolayer (scale bar: 25 µm). E) Schematic of the process for printing the tumor-on-a-chip prototype using various bioinks and other materials to construct CNC embedded and compartmentalized structures and allow for culture under dynamic conditions. F) Photograph of the printed chip directly used for CLM analysis without the need to disassemble. G) CLM tile scan of the printed tumor model with cancer (MCF-7) cells in the inner circle and endothelial (EAy.h926) cells in the outer circle, showing actin staining after 7 d of perfusion culture, (scale bar: 1 mm). H) Immunofluorescence images of endothelial cells forming cell–cell contact. I) MCF-7 clusters in the tumor-on-a-chip co-culture conditions in comparison with J) its equivalent monoculture (H, I, J scale bar: 25 µm). K) Cell cluster size in monoculture and tumor-on-a-chip co-culture. $p^{***} < 0.0001$, determined by unpaired t-test with Welch's correction. Images are representative of $n = 3$ independent experiments, data are means ± SD.

metal pins interfaced through the gasket walls, the CNC bath was fibrillated with Ca^{2+} and then the system was sealed and perfused for a period of one week to allow cell culture. Interestingly, cells showed homogeneous distributions (Movie S3, Supporting Information) and started to organize into a tubular monolayer (Figure 6B) with an open lumen covering the inner surface of the channel (Figure 6C,D). No invasion of cells into the fibrillar CNC matrix was noticed, suggesting that the perfusable vascular channels were able to maintain their structural integrity during cell culture under dynamic conditions Although paper-based microfluidic devices have been previously used for in vitro modeling of vascular tissues,[53] their fabrication and subsequent cell seeding requires several nonintegrated steps. In contrast, our approach allowed in situ endothelization whilst maintaining the self-standing structural integrity of the channel, in a simple and integrated single process.

Next, tumor models were selected as proof-of-concept scenarios to test the potential of this biofabrication platform to build multicellular OoC. Based on the design principles of state-of-the-art cancer models,[82] the proposed tumor-on-a-chip aimed to capture some morphological aspects of the cancer environment, namely the biochemical and biophysical cues deriving from the compartmentalized structure of the cancerous mass surrounded by the vascularized stroma. For this purpose, permeable chip gaskets were first printed on glass slides with a silicone elastomer ink, in which CNCs fluid gel was introduced for printing the cellular model (Figure 6F–H). Breast cancer cells (MCF-7) were bioprinted in the form of an inner ring surrounded by an outer ring of endothelial cells (EA.hy926). Gelatin was used as biocompatible fugitive ink to print peripheral channels around the cellular construct for perfusion of culture media. After sealing the system, fresh media was circulated for one week. The immunofluorescence images showed the development of MCF-7 clusters (Figure 6J) while endothelial cells tend to form extensive cell-to-cell contacts (Figure 6I), although well-developed networks were still not evident at this time point. Interestingly, the self-clustering of MCF-7 over time to form 3D microaggregates has been correlated with improved differentiation of these breast cancer cells[83] and is consistent with the signaling of angiocrine factors that regulate tumor growth in co-culture models.[84–86] The effects of this paracrine crosstalk in co-culture were well evident when comparing it with equivalent MCF-7 monoculture OoC systems (Figure 6K), where the size of formed cell clusters is significantly lower (Figure 6L). Although used here as a first proof-of-concept scenario, the results suggest that this OoC might be a promising platform for modeling tumor environments and should therefore be further explored with more detail in future functional studies.

3. Conclusions

The proposed CNC-based platform supports high-resolution printing of perfusable microfluidic channels and embedded constructs with arbitrary freeform 3D shapes using different low viscosity hydrogel bioinks and cell types. The controlled self-assembly of CNC after printing induces their fibrillation into networks that recreate the characteristic topography of native ECMs and allows the easy interstitial diffusion of macromolecules. It enables the direct writing of living constructs in the 3D space of a perfusable bioinspired housing material that allows diffusion of signaling biomolecules for cell–cell communications, using a simple extrusion 3D bioprinter without the need for specific microfabrication processes, equipment, or skills. The automated nature of this biofabrication platform further provides significant advantages of throughput, reproducibility, and scalability for the manufacturing of miniaturized multicellular systems with complex bioinspired 3D architectures. Additionally, the CNC matrix is transparent for real-time monitoring and embedded tissues can be easily harvested under mild biocompatible conditions by enzymatic digestion with cellulase for further offline processing. This unique set of properties in a single system has not been reported to date by previous support materials used in embedded 3D bioprinting and suggests that it can be a promising platform for the automated biofabrication of in vitro tissue/organ models, a concept that we have here preliminarily demonstrated for the manufacturing of OoC.

4. Experimental Section

Production and Tuning of CNC Fluid Gel Rheological Properties: The colloidal suspension of CNC was produced by acid hydrolysis of microcrystalline cellulose (Sigma-Aldrich) according to the previously optimized procedure[37] (detailed protocol is described in Supporting Information). For the production of the CNC fluid gel support bath, an initial 3 wt% CNC colloidal solution was sonicated for 1 min at 40% of amplitude output and then diluted to make nanoparticles suspensions with the desired concentration (1.5–2.5 wt%). For optimization of the printing process, crosslinking agent, i.e., calcium chloride solutions (Sigma-Aldrich), was added to CNC at varying concentrations (1.5×10^{-3}, 2.0×10^{-3}, 2.5×10^{-3}, and 7.5×10^{-3} м) to develop the fluid gel. After the addition of calcium chloride, the colloidal suspension was sonicated again for 1 min at 40% of amplitude output to ensure homogenous mixing. 500 µL of each prepared colloidal suspension was transferred to 1.5 mL Eppendorf tubes for the inversion test. After 10 minutes at rest, the tubes were inverted upside down to visually inspect the change in viscosity of the fluid gels formed.

The 2.5 wt% CNC concentration was chosen for further rheological evaluation. To measure the viscoelastic properties of the 2.5 wt% CNC colloidal suspension (0 and 2.0×10^{-3} м Ca^{2+}) and fibrillar matrix (7.5×10^{-3} м Ca^{2+}), 320 µL of each tested gel was poured on a parallel plate setup equipped with a geometry of 20 mm diameter and final gap of 1 mm between plates, using a Kinexus Pro Rheometer (Malvern Instruments, United Kingdom). The temperature was set at 37 °C and frequency 1 Hz. Shear viscosity was measured in response to shear rate (0.001 to 100 s^{-1}). Strain-dependent oscillatory shear rheology was determined at a fixed frequency of 1 Hz and strains between 0.1% and 200%. The self-healing properties of the CNC gels (2.0×10^{-3} м and 7.5×10^{-3} м Ca^{2+}) were measured by alternate strain cycles of 1% and 200% ($n = 3$ for all rheological measurements).

"Print-then-lock" Embedded Structures into CNC Fibrillar Matrix: For the embedded 3D printing experiments, 2.5 wt% CNC colloidal suspension with 2.0×10^{-3} м Ca^{2+} was chosen as a support matrix based on their shear-thinning and self-healing rheological properties. This fluid gel was first produced according to the aforementioned process and then poured into desired support mold or plate to be used for the printing process. BioX (Cellink, Sweden) with pneumatic printheads was used for 3D (bio)printing experiments. Computer-aided designs (CAD) were created using the free online software TINKERCAD and saved in stl (stereolithography) file format. The human femur was downloaded from NIH 3D Print Exchange (Model ID 3DPX-000168) while the human right kidney was acquired from Bioverse.com, both models were scaled down prior to their conversion into G-code. The stl to G-code conversion program PursaSlic3r 2.1 software was then used to slice the models into layers and translate the coordinates into commands. Cartridges of 3 mL were loaded with (bio)inks and 27G and 30G blunt needles were used as nozzles. The prints were performed applying pressures between 3 and 5 kPa with the printing speed of 5–8 mm s^{-1} (unless otherwise specified for specific ink or print). After 2–3 min postprinting, the support fluid gel was converted into a fibrillar matrix by inducing the hierarchical self-assembly of CNC through the addition of an excess of 7.5×10^{-3} м Ca^{2+} solution on top of the constructs, hardening it into stable hydrogels and locking the embedded 3D structures in place. After 30 min, the Ca^{2+} solution was removed and changed by phosphate buffer saline (PBS, Sigma-Aldrich), where the embedded prints were maintained until further analysis or cell-cultured following the procedures described below.

Preparation and Printing in Agarose Slurry: The agarose bath was produced by autoclaving 0.5 wt% Agarose (SeaKem, Lonza, USA) with 11×10^{-3} м $CaCl_2$ (Sigma-Aldrich) followed by cooling at constant magnetic stirring at 700 rpm to form agarose microparticles.[52] Then, the solution was poured into the desired mold to be used for embedded printing. The desired structures were directly fabricated in the agarose support bath following the same printing protocols described above for CNC fluid gel.

Preparation of Acellular Inks: The solution of 10 wt% and 5 wt% gelatin (type-A, porcine skin, Sigma-Aldrich) were prepared in PBS (Sigma-Aldrich) and their pH was adjusted to 7.4 before further use. For the preparation of enzymatically crosslinked gelatin 5 wt% ink

(GelTG), the colloidal CNC suspension was supplemented with 2 wt% transglutaminase enzyme (Ajinomoto, Japan).[47] To prepare the alginate ink, sodium alginate (Sigma-Aldrich) 2 wt% was dissolved in PBS and stirred at room temperature for 48 h. GelMA was synthesized following the pre-established protocol[87] by reacting gelatin (type-A, porcine skin, Sigma-Aldrich) with methacrylic anhydride (Sigma-Aldrich). For the preparation of the photocrosslinkable ink, 5 wt% GelMA was dissolved in PBS with 0.5% Irgacure 2959 (Sigma-Aldrich). Inbuilt 365 nm light module in BioX printer was used for 3 min and at a distance of 3 cm from the light module for GelMA photocuring after printing. To aid the visualization of printed structures in photographs and transmitted light microscopy images during the optimization and characterization steps, food color dyes were added into the inks, while for confocal laser microscopy (CLM) fluorescein isothiocyanate–dextran 250 kDa (Sigma-Aldrich) was added into the ink prior to printing. Gelatin 5 wt% and pluronic F-127 25 wt% (Sigma-Aldrich) were used as sacrificial inks in the printing of perusable constructs, depending on the assay.

Diffusional Permeability Assay: To determine the diffusional permeability of biomolecules through the CNC fibrillar matrix, hollow channels were fabricated using pluronic F-127 as fugitive ink. The printed channels were locked by the addition of 7.5×10^{-3} M calcium chloride solution and the fugitive ink was purged after liquefaction by placing the fabricated structure at 4 °C. Then, aqueous solutions (25 µg mL^{-1}) of 4 kDa or 250 kDa dextran-FITC (Sigma-Aldrich, USA) were separately injected into the channel, and samples were immediately observed by fluorescence microscopy (Axio Observer, Zeiss, Germany). The diffusion of the dextran with different molecular sizes over time (up to 60 min) was analyzed by quantification of spatial changes in mean fluorescence intensity on the acquired images plotted against the distance from the center of the channel.

Cell Isolation and Culture: Human adipose stem cells (hASCs) were obtained from lipoaspirate samples of the abdominal region after informed consent of patients undergoing plastic surgery, under the scope of protocols established with Hospital da Prelada (Porto, Portugal) with the approval of the Hospital and University of Minho Ethics Committees (approval numbers 005/2019 and 014/2019, respectively). hASCs were isolated according to the previously optimized protocol.[88,89] Alpha modified Eagle medium (alpha-MEM) supplemented with 10 vol% fetal bovine serum (FBS, Thermo Fisher Scientific) and 1 vol% penicillin/streptomycin solution (Sigma-Aldrich) was used to maintain cells in culture. hASCs were not used beyond passage 8. Human umbilical vein endothelial cells (HUVEC) were obtained from ThermoFisher Scientific and maintained in culture using EndoGRO-MV media (Sigma-Aldrich). HUVEC were not used beyond passage 6. MCF-7 breast cancer cell line was purchased from Sigma-Aldrich and maintained in culture using high glucose Dulbecco's modified Eagle medium (DMEM, Gibco) supplemented with 10% FBS (Thermo Fisher Scientific) and 1% antibiotic/antimycotic solution (Sigma-Aldrich). The endothelial cell line EA.hy926 (ATCC CRL-2922) was also commercially obtained from (ATCC, LGC Standards, UK) and maintained in culture using low glucose Dulbecco's modified Eagle medium (DMEM, Gibco) supplemented with 10% FBS (Thermo Fisher Scientific) and 1% antibiotic/antimycotic solution (Sigma-Aldrich).

Preparation of Bioinks: Two bioink hydrogels were used for the bioprinting of cellular constructs: GelTG and platelet lysate (PL). The GelTG bioink was prepared by adding cell suspension to a gelatin 10 wt% in PBS (Sigma-Aldrich) and adjusting the final gelatin concentration to 5 wt%. For the preparation of PL bioinks, platelet concentrates were obtained from healthy human blood donors, provided by Serviço de Imuno-Hemoterapia of Centro Hospitalara de S. João, EPE (Porto, Portugal) under an approved institutional board protocol (ethical commission of CHSJ/FMUP approved at 18/13/2018). PL was produced according to the previously established protocol.[50] Briefly, the samples of platelet concentrate were pooled from 12 healthy human donors and subjected to three freeze-thaw cycles consisting of freezing by immersion in liquid nitrogen followed by heating at 37 °C in the water bath. The produced PL was aliquoted and stored at −80 °C until further use. The frozen aliquots were thawed at 37 °C for 5 min, centrifuged at 4000 G for 5 min (Centrifuge 5810 R, Eppendorf) and then filtered with a 0.45 µm pore membrane filter prior to being mixed with the trypsinized cell pellets, resulting in the final PL bioinks used for bioprinting.

Fabrication of Microphysiological Systems Embedded in CNC Matrix: hASCs suspended in GelTG or PL hydrogels at a cell density of 6×10^6 cells mL^{-1} were used as bioinks for the fabrication of representative microphysiological systems with selected 3D configuration following the optimized procedures described for printing with acellular inks. Both multiwell plates (for tissue plate demonstration) or cell culture µ-Dish (Ibidi, Germany) were used as a support platform for the prints, depending on the assay. After printing, the fabricated structures were locked with 7.5×10^{-3} M calcium chloride solution, kept in a cell incubator for 30 min, and then excess calcium chloride solution was replaced by culture media. All the constructs printed with GelTG and PL bioinks were cultured up to 4 weeks under standard culture condition (alpha-MEM with 10% FBS) except the miniatured human femur bone biofabricated with PL bioinks, which was maintained in culture using alpha-MEM without supplementation of FBS following the xenofree culture conditions we have previously proposed.[50] The media was changed every alternate day. (n = 3 for biologically independent experiments).

Harvesting of 3D Constructs from the CNC Fibrillar Matrix: Cellulase from *Trichoderma reesei*[68] (Sigma-Aldrich) at a concentration of 23 g L^{-1} in PBS or culture media was used for enzymatic hydrolysis of CNC matrix and thus harvest the acellular or bioprinted constructs, respectively. The enzyme was sterile filtered prior to use for releasing the bioprinted construct. After 24 h of incubation at 37 °C, the released structure was washed with PBS and processed for further analysis.

Multimaterial Bioprinting of Dynamic OoC Systems: For fabricating perfusion chips, outer silicone gaskets were 3D printed on glass slides with DOWSIL TORAY SE 1700 (DOW, USA) in a polymer and curing agent proportion of 10:1 using BioX (25G plastic conical needle as a nozzle, pressure of 120 kPa, printing speed of 20 mm s^{-1}). After printing, the silicone gaskets were kept at 100 °C for 4 h for curing. The same procedures described in previous sections were applied for bioprinting with the different bioinks on CNC fluid gel at 5 kPa and 5.0 mm s^{-1} using 27G blunt needles as a nozzle. For fabrication of perfusable vascular channels, HUVECs in gelatin 5 wt% solutions dissolved in EndoGRO-MV at a density of 8×10^6 cells per mL were used as bioink to print a single channel of 18 mm length and 200 µm diameter. After 2–3 min, the structure was locked with 7.5×10^{-3} M calcium chloride solution, sealed with a glass slide on top of the built construction that was afterward fixed on a custom support frame 3D printed using poly-lactic acid (PLA, Mitsubishi Chemicals Performance Polymers, USA) in a B2 × 300 3D printer (BEEVERYCREATIVE, Portugal), and placed in a cell incubator for liquefaction of gelatin. The perfusion chip was flipped every 10 min for 30 min to avoid cell sedimentation. After 2 h of incubation, the channel was perfused with EndoGRO-MV media by connecting a peristaltic pump to metallic connectors (attached to the perfusion chip as inlet and outlet for media) with a flow rate of 40 µL min^{-1}. The perfusion chip was kept in dynamic culture for a period of 2 weeks (see the assembled setup in Figure S6, Supporting Information).

Similar bioprinting procedures were applied for fabricating the tumor-on-a-chip model. After printing the external gasket and filling it with CNC fluid gel, a circular shaped model was fabricated by first printing the inner ring with MCF-7 cancer cells at a density of 6×10^6 cells mL^{-1} in PL, and then EA.hy926 endothelial cells suspended in gelatin 5 wt%/PL (3:1 v/v) at a density of 8×10^6 cells mL^{-1} was used as bioink to print the in outer cell rings. After printing the cell structures, gelatin 5 wt% solution was used as fugitive ink to print an open external channel allowing the circulation of culture media in the periphery of the fabricated cellular construct. The CNC was then fibrillated, and the bioprinted chip was sealed and connected to a peristaltic pump for perfusion, as described above. After incubating the chip at 37 °C, the liquefied fugitive ink was purged and then the system was kept in dynamic culture over the period of one week at a flow rate of 40 µL min^{-1}. ($n = 3$, biologically independent experiments).

Fluorescence Stainings: All fluorescent stainings were performed on cell constructs embedded within the CNC matrix except for the samples in perfused systems. In this case, similar staining protocols were followed but instead of adding reagents in static conditions, all the reagents were perfused stepwise via a peristaltic pump. Cell viability on the bioprinted constructs was assessed by staining cells with Calcein AM (Thermo Fisher Scientific) 1:500 dilution in culture media and propidium iodide (Thermo Fisher Scientific) 1:1000 dilution in PBS to stain live and dead cells, respectively, on days 1, 3, 7, and 14 for hASCs and day 14 for HUVECs. To track hASCs within different compartments after printing, cells were labeled with CellTracker Deep Red Dye or CellTracker Green CMFDA Dye (ThermoFisher Scientific) following the manufacturer's instructions prior to suspending it in the respective bioink hydrogel to aid in visualization after bioprinting. For cell cytoskeleton staining and immunolabeling, the samples were first washed with PBS three times and 4% paraformaldehyde (Thermo Fisher Scientific) was used to fix the cells for 30 minutes at room temperature. Then the cell membrane was permeabilized with 0.2% Triton X-100 in PBS for 1 h at room temperature. Afterward, the samples were blocked in 1% (w/v) BSA in PBS for 1 h at room temperature. F-actin fibers were stained with phalloidin conjugated with rhodamine (Sigma-Aldrich, 1:200 dilution) in PBS, and nuclei were stained with 4',6-diamidino-2-phenylindole (DAPI, Sigma-Aldrich, 1:1000 dilution) in PBS. In the tumor-on-chip, endothelial cells were immunolabeled with anti-CD31(PECAM-1)-APC antibody (Thermo Fisher Scientific, 1:200 dilution) in 1 wt% BSA solution for 1 h at room temperature. Then F-actin fibers were stained with phalloidin conjugated with fluorescein isothiocyanate (Sigma-Aldrich) and nuclei were counterstained with DAPI. Confocal laser microscope TCS SP8 (Leica Microsystems, Germany) was used for fluorescence imaging acquired directly from the constructions embedded in the CNC matrix. ImageJ was used to quantify the proliferative density of cells and for the characterization of the size distribution of cell aggregates. Proliferative density was estimated from corresponding cells' area occupied in selected regions of interest (ROI). The area of cell aggregates was manually defined by their outer boundaries. Results are provided as mean ± standard deviation ($n = 3$, independent experiments).

Scanning Electron Microscopy (SEM) and Transmission Electron Microscopy (STEM): The morphology of CNC was analyzed via STEM (Auriga Compact, Zeiss). For sample preparation a drop of 0.0015 wt% CNC solution was placed on TEM grids (Carbon Type B, 400 M Cu, Monocomp). Images were acquired with an acceleration voltage from 25 to 30 kV. The microstructure of the CNC fibrillar matrix was observed by high-resolution SEM (JSM-6010LV, JEOL, Japan). Before analysis, CNC hydrogels were critical point dried after solvent exchange from water to ethanol with ethanol gradient from 10 to 99.9 vol%, and then ethanol was replaced with liquefied CO_2 using critical point dryer (Autosamdri-815 Series-A Tousimis). To expose the inner structure of dried samples, they were freeze-fractured after immersion in liquid nitrogen. Before analysis, the samples were sputter-coated with platinum (Cressington Scientific Instruments). The images were collected with an acceleration voltage from 2 to 10 kV. Image analysis was performed using ImageJ software. Results are provided as mean ± standard deviation ($n = 3$, independent experiments).

Statistical Analysis: The statistical analysis was performed in GraphPad Prism 6 software. Two-way ANOVA followed by Tukey's post hoc tests was used for the analysis of variance between multiple groups while unpaired two-tailed Student's *t*-tests with Welch's correction was used for comparisons between two experimental groups. Results are provided as mean ± standard deviation of $n \geq 3$ independent experiments. Values were considered significant when $p < 0.05$.

Supporting Information

Supporting Information is available from the Wiley Online Library or from the author.

Acknowledgements

The authors thank Hospital da Prelada (Porto, Portugal) for providing adipose tissue samples and Hospital São João (Porto, Portugal) for providing platelet concentrates. The authors acknowledge the financial support from project NORTE-01-0145- FEDER-000021 supported by Norte Portugal Regional Operational Program (NORTE 2020), under the PORTUGAL 2020 Partnership Agreement, through the European Regional Development Fund (ERDF); the European Union Framework Program for Research and Innovation HORIZON 2020, under the Twinning grant agreement no. 810850– Achilles, European Research Council grant agreement no. 772817, Fundação para a Ciência e a Tecnologia for the PhD grant for S.M.B PD/BD/129403/2017 financed through doctoral program in Tissue Engineering, Regenerative Medicine and Stem Cells (TERM&SC), and project PTDC/NAN-MAT/30595/2017. Schematics in Figures 1, 2, and 6 were created with BioRender.com. The authors thank Milan Sixt and Bárbara B. Mendes for preliminary tests with CNC fluid gel. The authors thank David Caballero, Catarina Abreu, and Mandana Mombeinipour for providing endothelial cells and Virginia Brancato for breast cancer cells.

Conflict of Interest

The authors declare no conflict of interest.

Data Availability Statement

Research data are not shared.

Keywords

cellulose nanocrystals, embedded bioprinting, fibrillar matrix, microphysiological systems, self-assembly

Received: May 5, 2021
Revised: July 27, 2021
Published online: August 11, 2021

---

[1] C. Mota, S. Camarero-Espinosa, M. B. Baker, P. Wieringa, L. Moroni, *Chem. Rev.* **2020**, *120*, 10547.
[2] S. N. Bhatia, D. E. Ingber, *Nat. Biotechnol.* **2014**, *32*, 760.
[3] B. Zhang, A. Korolj, B. F. L. Lai, M. Radisic, *Nat. Rev. Mater.* **2018**, *3*, 257.
[4] D. E. Ingber, *Adv. Sci.* **2020**, 7, 2002030.
[5] J. Parrish, K. Lim, B. Zhang, M. Radisic, T. B. F. Woodfield, *Trends Biotechnol.* **2019**, *37*, 1327.
[6] S. B. Campbell, Q. Wu, J. Yazbeck, C. Liu, S. Okhovatian, M. Radisic, *ACS Biomater. Sci. Eng.* **2021**, *7*, 2880.
[7] S. Rajasekar, D. S. Y. Lin, L. Abdul, A. Liu, A. Sotra, F. Zhang, B. Zhang, *Adv. Mater.* **2020**, *32*, 2002974.
[8] E. Prince, E. Kumacheva, *Nat. Rev. Mater.* **2019**, *4*, 99.
[9] V. S. LeBleu, B. MacDonald, R. Kalluri, *Exp. Biol. Med.* **2007**, *232*, 1121.
[10] C. J. Murphy, Z.-Y. Wang, P. F. Nealey, D. E. Bjorling, G. A. Abrams, *Urol. Res.* **2003**, *31*, 341.
[11] M. A. Morrissey, D. R. Sherwood, *J. Cell Sci.* **2015**, *128*, 1661.
[12] C. Frantz, K. M. Stewart, V. M. Weaver, *J. Cell Sci.* **2010**, *123*, 4195.
[13] T. Rozario, D. W. DeSimone, *Dev. Biol.* **2010**, *341*, 126.
[14] S. Gholizadeh, Z. Allahyari, R. N. Carter, L. F. Delgadillo, M. Blaquiere, F. Nouguier-Morin, N. Marchi, T. R. Gaborski, *Adv. Mater. Technol.* **2020**, *5*, 2000474.

[15] J. Laurent, G. Blin, F. Chatelain, V. Vanneaux, A. Fuchs, J. Larghero, M. Théry, *Nat. Biomed. Eng.* **2017**, *1*, 939.
[16] C. L. Hedegaard, A. Mata, *Biofabrication* **2020**, *12*, 032002.
[17] W. Zhang, Y. S. Zhang, M. Bakht, J. Aleman, S.-R. Shin, K. Yue, M. Sica, J. Ribas, M. Duchamp, J. Ju, R. Banan Sadeghian, D. Kim, M. Dokmeci, A. Atala, A. Khademhosseini, *Lab Chip* **2016**, *16*, 1579.
[18] M. Duchamp, S. M. Bakht, J. Ju, I. K. Yazdi, W. Zhang, Y. S. Zhang, *Adv. Mater. Technol.* **2019**, *4*, 1800741.
[19] A. K. Miri, E. Mostafavi, D. Khorsandi, S.-K. Hu, M. Malpica, A. Khademhosseini, *Biofabrication* **2019**, *11*, 042002.
[20] R. Levato, T. Jungst, R. G. Scheuring, T. Blunk, J. Groll, J. Malda, *Adv. Mater.* **2020**, *32*, 1906423.
[21] H. H. Susapto, D. Alhattab, S. Abdelrahman, Z. Khan, S. Alshehri, K. Kahin, R. Ge, M. Moretti, A. H. Emwas, C. A. E. Hauser, *Nano Lett.* **2021**, *21*, 2719.
[22] Y. Wu, G. M. Fortunato, B. O. Okesola, F. L. P. Di Brocchetti, R. Suntornnond, J. Connelly, C. De Maria, J. C. Rodriguez-Cabello, G. Vozzi, W. Wang, A. Mata, *Biofabrication* **2021**, *13*, 35027.
[23] Y. Wu, B. O. Okesola, J. Xu, I. Korotkin, A. Berardo, I. Corridori, F. L. P. di Brocchetti, J. Kanczler, J. Feng, W. Li, Y. Shi, V. Farafonov, Y. Wang, R. F. Thompson, M. M. Titirici, D. Nerukh, S. Karabasov, R. O. C. Oreffo, J. Carlos Rodriguez-Cabello, G. Vozzi, H. S. Azevedo, N. M. Pugno, W. Wang, A. Mata, *Nat. Commun.* **2020**, *11*, 1.
[24] A. McCormack, C. B. Highley, N. R. Leslie, F. P. W. Melchels, *Trends Biotechnol.* **2020**, *38*, 584.
[25] R. M. A. Domingues, M. E. Gomes, R. L. Reis, *Biomacromolecules* **2014**, *15*, 2327.
[26] M. Chau, S. E. Sriskandha, D. Pichugin, H. Thérien-Aubin, D. Nykypanchuk, G. Chauve, M. Méthot, J. Bouchard, O. Gang, E. Kumacheva, *Biomacromolecules* **2015**, *16*, 2455.
[27] O. Jeon, Y. Bin Lee, H. Jeong, S. J. Lee, D. Wells, E. Alsberg, *Mater. Horiz.* **2019**, *6*, 1625.
[28] C. D. Morley, S. T. Ellison, T. Bhattacharjee, C. S. O'Bryan, Y. Zhang, K. F. Smith, C. P. Kabb, M. Sebastian, G. L. Moore, K. D. Schulze, S. Niemi, W. G. Sawyer, D. D. Tran, D. A. Mitchell, B. S. Sumerlin, C. T. Flores, T. E. Angelini, *Nat. Commun.* **2019**, *10*, 3029.
[29] C. B. Highley, C. B. Rodell, J. A. Burdick, *Adv. Mater.* **2015**, *27*, 5075.
[30] A. C. Daly, M. D. Davidson, J. A. Burdick, *Nat. Commun.* **2021**, *12*, 753.
[31] B. Ayan, D. N. Heo, Z. Zhang, M. Dey, A. Povilianskas, C. Drapaca, I. T. Ozbolat, *Sci. Adv.* **2020**, 6, eaaw5111.
[32] J. L. Puetzer, T. Ma, I. Sallent, A. Gelmi, M. M. Stevens, *Biomaterials* **2021**, *269*, 120527.
[33] B. B. Mendes, M. Gómez-Florit, R. A. Pires, R. M. A. Domingues, R. L. Reis, M. E. Gomes, *Nanoscale* **2018**, *10*, 17388.
[34] R. Ajdary, B. L. Tardy, B. D. Mattos, L. Bai, O. J. Rojas, *Adv. Mater.* **2021**, 33, 2001085.
[35] S. Shafiei-Sabet, W. Y. Hamad, S. G. Hatzikiriakos, *Langmuir* **2012**, *28*, 17124.
[36] J. Yang, F. Xu, C. R. Han, *Biomacromolecules* **2017**, *18*, 1019.
[37] S. Araújo-Custódio, M. Gomez-Florit, A. R. Tomás, B. B. Mendes, P. S. Babo, S. M. Mithieux, A. Weiss, R. M. A. Domingues, R. L. Reis, M. E. Gomes, *ACS Biomater. Sci. Eng.* **2019**, *5*, 1392.
[38] B. B. Mendes, M. Gómez-Florit, H. Osório, A. Vilaça, R. M. A. Domingues, R. L. Reis, M. E. Gomes, *Chem. Commun.* **2020**, *56*, 6882.
[39] R. M. A. Domingues, M. Silva, P. Gershovich, S. Betta, P. Babo, S. G. Caridade, J. F. Mano, A. Motta, R. L. Reis, M. E. Gomes, *Bioconjugate Chem.* **2015**, *26*, 1571.
[40] S. Shafiei-Sabet, W. Y. Hamad, S. G. Hatzikiriakos, *Cellulose* **2014**, *21*, 3347.
[41] C. Bruel, J. R. Tavares, P. J. Carreau, M. C. Heuzey, *Carbohydr. Polym.* **2019**, *205*, 184.
[42] M. H. Chen, L. L. Wang, J. J. Chung, Y. H. Kim, P. Atluri, J. A. Burdick, *ACS Biomater. Sci. Eng.* **2017**, *3*, 3146.
[43] L. Lewis, M. Derakhshandeh, S. G. Hatzikiriakos, W. Y. Hamad, M. J. MacLachlan, *Biomacromolecules* **2016**, *17*, 2747.
[44] A. K. Grosskopf, R. L. Truby, H. Kim, A. Perazzo, J. A. Lewis, H. A. Stone, *ACS Appl. Mater. Interfaces* **2018**, *10*, 23353.
[45] M. Mobaraki, M. Ghaffari, A. Yazdanpanah, Y. Luo, D. K. Mills, *Bioprinting* **2020**, *18*, e00080.
[46] F. L. C. Morgan, L. Moroni, M. B. Baker, *Adv. Healthcare Mater.* **2020**, *9*, 1901798.
[47] A. M. Compaan, K. Song, Y. Huang, *ACS Appl. Mater. Interfaces* **2019**, *11*, 5714.
[48] J. J. Senior, M. E. Cooke, L. M. Grover, A. M. Smith, *Adv. Funct. Mater.* **2019**, *29*, 1904845.
[49] S. R. Moxon, M. E. Cooke, S. C. Cox, M. Snow, L. Jeys, S. W. Jones, A. M. Smith, L. M. Grover, *Adv. Mater.* **2017**, *29*, 1605594.
[50] B. B. Mendes, M. Gómez-Florit, A. G. Hamilton, M. S. Detamore, R. M. A. Domingues, R. L. Reis, M. E. Gomes, *Biofabrication* **2020**, *12*, 015012.
[51] A. Lee, A. R. Hudson, D. J. Shiwarski, J. W. Tashman, T. J. Hinton, S. Yerneni, J. M. Bliley, P. G. Campbell, A. W. Feinberg, *Science* **2019**, *365*, 482.
[52] S. E. Park, A. Georgescu, D. Huh, *Science* **2019**, *364*, 960.
[53] F. Cheng, X. Cao, H. Li, T. Liu, X. Xie, D. Huang, S. Maharjan, H. P. Bei, A. Gómez, J. Li, H. Zhan, H. Shen, S. Liu, J. He, Y. S. Zhang, *Nano Lett.* **2019**, *19*, 3603.
[54] S. Shin, J. Hyun, *ACS Appl. Mater. Interfaces* **2017**, *9*, 26438.
[55] A. Skardal, S. V. Murphy, M. Devarasetty, I. Mead, H. W. Kang, Y. J. Seol, Y. S. Zhang, S. R. Shin, L. Zhao, J. Aleman, A. R. Hall, T. D. Shupe, A. Kleensang, M. R. Dokmeci, S. Jin Lee, J. D. Jackson, J. J. Yoo, T. Hartung, A. Khademhosseini, S. Soker, C. E. Bishop, A. Atala, *Sci. Rep.* **2017**, *7*, 8837.
[56] S. S. Bale, L. Vernetti, N. Senutovitch, R. Jindal, M. Hegde, A. Gough, W. J. McCarty, A. Bakan, A. Bhushan, T. Y. Shun, I. Golberg, R. DeBiasio, O. B. Usta, D. L. Taylor, M. L. Yarmush, *Exp. Biol. Med.* **2014**, *239*, 1180.
[57] K. J. De France, T. Hoare, E. D. Cranston, *Chem. Mater.* **2017**, *29*, 4609.
[58] S. F. Badylak, *Biomaterials* **2007**, *28*, 3587.
[59] T. M. Keenan, A. Folch, *Lab Chip* **2008**, *8*, 34.
[60] K. T. Lawlor, J. M. Vanslambrouck, J. W. Higgins, A. Chambon, K. Bishard, D. Arndt, P. X. Er, S. B. Wilson, S. E. Howden, K. S. Tan, F. Li, L. J. Hale, B. Shepherd, S. Pentoney, S. C. Presnell, A. E. Chen, M. H. Little, *Nat. Mater.* **2021**, *20*, 260.
[61] Y. Zheng, J. Chen, J. A. López, *Nat. Commun.* **2015**, *6*, 7858.
[62] T. Bhattacharjee, S. M. Zehnder, K. G. Rowe, S. Jain, R. M. Nixon, W. G. Sawyer, T. E. Angelini, *Sci. Adv.* **2015**, *1*, e1500655.
[63] N. Noor, A. Shapira, R. Edri, I. Gal, L. Wertheim, T. Dvir, *Adv. Sci.* **2019**, 6, 1900344.
[64] G. Cidonio, M. Cooke, M. Glinka, J. I. Dawson, L. Grover, R. O. C. Oreffo, *Mater. Today Bio* **2019**, *4*, 100028.
[65] G. Luo, Y. Yu, Y. Yuan, X. Chen, Z. Liu, T. Kong, *Adv. Mater.* **2019**, *31*, 1904631.
[66] P. N. Bernal, P. Delrot, D. Loterie, Y. Li, J. Malda, C. Moser, R. Levato, *Adv. Mater.* **2019**, 31, e1904209.
[67] B. Grigoryan, S. J. Paulsen, D. C. Corbett, D. W. Sazer, C. L. Fortin, A. J. Zaita, P. T. Greenfield, N. J. Calafat, J. P. Gounley, A. H. Ta, F. Johansson, A. Randles, J. E. Rosenkrantz, J. D. Louis-Rosenberg, P. A. Galie, K. R. Stevens, J. S. Miller, *Science* **2019**, *364*, 458.
[68] J. G. Torres-Rendon, M. Köpf, D. Gehlen, A. Blaeser, H. Fischer, L. De Laporte, A. Walther, *Biomacromolecules* **2016**, *17*, 905.
[69] Q. Gu, E. Tomaskovic-Crook, R. Lozano, Y. Chen, R. M. Kapsa, Q. Zhou, G. G. Wallace, J. M. Crook, *Adv. Healthcare Mater.* **2016**, *5*, 1429.
[70] Y. Xin, G. Chai, T. Zhang, X. Wang, M. Qu, A. Tan, M. Bogari, M. Zhu, L. Lin, Q. Hu, Y. Liu, Y. Zhang, *Biomed. Rep.* **2016**, *5*, 723.

[71] M. L. Bedell, A. M. Navara, Y. Du, S. Zhang, A. G. Mikos, *Chem. Rev.* **2020**, *120*, 10744.

[72] A. Ovsianikov, A. Khademhosseini, V. Mironov, *Trends Biotechnol.* **2018**, *36*, 348.

[73] M. A. Skylar-Scott, S. G. M. Uzel, L. L. Nam, J. H. Ahrens, R. L. Truby, S. Damaraju, J. A. Lewis, *Sci. Adv.* **2019**, *5*, eaaw2459.

[74] A. Daly, M. Davidson, J. Burdick, *Nat. Commun.* **2021**, *12*, 753.

[75] D. B. Gehlen, N. Jürgens, A. Omidinia-Anarkoli, T. Haraszti, J. George, A. Walther, H. Ye, L. De Laporte, *Macromol. Rapid Commun.* **2020**, *41*, 2000191.

[76] L. A. Low, C. Mummery, B. R. Berridge, C. P. Austin, D. A. Tagle, *Nat. Rev. Drug Discovery* **2021**, 20, 345.

[77] Q. Zhong, H. Ding, B. Gao, Z. He, Z. Gu, *Adv. Mater. Technol.* **2019**, *4*, 1800663.

[78] J. A. Brassard, M. Nikolaev, T. Hübscher, M. Hofer, M. P. Lutolf, *Nat. Mater.* **2021**, *20*, 22.

[79] A. K. Miri, E. Mostafavi, D. Khorsandi, S. K. Hu, M. Malpica, A. Khademhosseini, *Biofabrication* **2019**, *11*, 042002.

[80] L. Ouyang, J. P. K. Armstrong, Q. Chen, Y. Lin, M. M. Stevens, *Adv. Funct. Mater.* **2020**, *30*, 1908349.

[81] V. K. Lee, D. Y. Kim, H. Ngo, Y. Lee, L. Seo, S. S. Yoo, P. A. Vincent, G. Dai, *Biomaterials* **2014**, *35*, 8092.

[82] H. G. Yi, Y. H. Jeong, Y. Kim, Y. J. Choi, H. E. Moon, S. H. Park, K. S. Kang, M. Bae, J. Jang, H. Youn, S. H. Paek, D. W. Cho, *Nat. Biomed. Eng.* **2019**, *3*, 509.

[83] T. Jiang, J. G. Munguia-Lopez, S. Flores-Torres, J. Grant, S. Vijayakumar, A. De Leon-Rodriguez, J. M. Kinsella, *Sci. Rep.* **2017**, *7*, 1.

[84] P. Datta, M. Dey, Z. Ataie, D. Unutmaz, I. T. Ozbolat, *npj Precis. Oncol.* **2020**, *4*, 1.

[85] M. M. Vantangoli, S. J. Madnick, S. M. Huse, P. Weston, K. Boekelheide, *PLoS One* **2015**, *10*, e0135426.

[86] J. M. Butler, H. Kobayashi, S. Rafii, *Nat. Rev. Cancer* **2010**, *10*, 138.

[87] A. I. Van Den Bulcke, B. Bogdanov, N. De Rooze, E. H. Schacht, M. Cornelissen, H. Berghmans, *Biomacromolecules* **2000**, *1*, 31.

[88] G. Yu, Z. E. Floyd, X. Wu, Y. D. C. Halvorsen, J. M. Gimble, *Methods Mol. Biol.* **2011**, *702*, 17.

[89] P. P. Carvalho, X. Wu, G. Yu, I. R. Dias, M. E. Gomes, R. L. Reis, J. M. Gimble, *Cells Tissues Organs* **2011**, *194*, 494.